# Nanocluster and Single-Atom Catalysts for Thermocatalytic Conversion of CO and CO$_2$

| | |
|---|---|
| Journal: | *Catalysis Science & Technology* |
| Manuscript ID | CY-MRV-06-2020-001316.R1 |
| Article Type: | Minireview |
| Date Submitted by the Author: | 03-Aug-2020 |
| Complete List of Authors: | Doherty, Francis; University of Michigan College of Engineering, Chemical Engineering; University of Michigan, Catalysis Science and Technology Institute<br>Wang, Hui; Tianjin University, School of Chemical Engineering & Technology<br>Yang, Ming; General Motors Global R&D, Chemical and Materials Systems Laboratory; Clemson University, Department of Chemical and Biomolecular Engineering<br>Goldsmith, Bryan; University of Michigan, Chemical Engineering; University of Michigan, Catalysis Science and Technology Institute |
| | |

# Nanocluster and Single-Atom Catalysts for Thermocatalytic Conversion of CO and CO₂

Francis Doherty,[1,2,^] Hui Wang,[3,^] Ming Yang,[4,5*] Bryan R. Goldsmith[1,2*]

*[1]Department of Chemical Engineering, University of Michigan, Ann Arbor, MI, USA. [2]Catalysis Science and Technology Institute, University of Michigan, Ann Arbor, MI, USA. [3]International Joint Research Laboratory of Materials Microstructure, Institute for New Energy Materials & Low Carbon Technologies, School of Materials Science and Engineering, Tianjin University of Technology, Tianjin, China. [4]Chemical and Materials Systems Laboratory, General Motors Global Research and Development, Warren, MI, USA. [5]Department of Chemical and Biomolecular Engineering, Clemson University, Clemson, SC, USA.*

*^F. Doherty and H. Wang have contributed equally to this article.*

*Corresponding authors e-mail: myang3@clemson.edu; bgoldsm@umich.edu*

## Abstract

In this Minireview, we discuss recent advances in understanding nanocluster and single-atom catalysts for CO and CO₂ emissions control applications. Through analyzing thermocatalytic CO oxidation and CO₂ reduction, two fundamentally and industrially important reactions, we compare representative nanocluster and single-atom catalytic systems from perspectives of intrinsic chemistry and reaction engineering. Generally, nanoclusters and single atoms display different catalytic performances (i.e., activity, selectivity, and stability) for these reactions depending on the synthesis methods, support materials, and reaction conditions. Key observations of activity and selectivity tradeoffs between nanoclusters and single-atom catalysts are highlighted. The dynamic structural responses of these catalytic species under CO oxidation or CO₂ reduction reaction conditions are also discussed. Synthetic control and detailed experimental and computational characterization of single-atom and nanocluster catalysts for CO and CO₂ conversion have led to exciting progress over the past decade. Still, more efforts are needed to understand and develop catalysts that meet the environmental, energy, and technical requirements to power a sustainable global economy.

## 1. Introduction

Heterogeneous catalysis is an empowering technology used in environmental applications to mitigate greenhouse gas emissions. For over a century,[1,2] the exploration of active, stable, and cost-effective supported metal catalysts has driven fundamental and industrial catalysis research to sustainably convert ubiquitous emissions such as CO and CO₂. The development of catalytic converter technology has been pivotal for the automotive industry to comply with ever-tightening air quality regulations.[3] CO oxidation is an important reaction in vehicle emissions control and also serves as an informative probe reaction to connect catalyst properties and structures with the catalytic performance and reaction pathways.[3–6] Another significant reaction for emissions control is thermocatalytic CO₂ reduction to CO via the reverse water gas shift reaction.[7–9] CO can then be used as a feedstock for Fischer-Tropsch synthesis[10,11] or alternative processes involving electrocatalysis[12,13] or plasma catalysis[14] to create value-added C₂₊ chemicals with potentially less

environmental impact. Alternative technologies to steam methane reforming such as water splitting have the potential to decrease the carbon footprint for generating $H_2$ and thus make thermocatalytic $CO_2$ reduction a more environmentally sustainable process.

Precious metals are active catalytic components for the conversion of CO and $CO_2$, but the high global demand for such reactions requires low catalyst loadings of these metals because of their scarcity and high cost. Nanoclusters (~1 nm) and single atoms (**Fig. 1a**) provide nearly 100% atom efficiency for a specified reaction and therefore are desirable from an atom economy viewpoint.[15,16] For many reactions, nanoclusters have higher intrinsic activity than their larger nanoparticle counterparts, in large part due to their undercoordinated nature and increased prevalence of corner and edge sites. **Fig. 1b** shows a typical relationship between particle diameter and the fraction of corner, edge, and surface (terrace) atoms in a representative supported particle, highlighting that the fraction of corner and edge sites increases as particle diameter decreases.[17] Additionally, single atoms can display catalytic properties far removed from their nanocluster counterparts because of their unique electronic properties and coordination environment. The discussion of similarities and differences between supported single-atom and nanocluster catalysts has garnered much attention.[16,18–20] Nonetheless, the reasons underlying the differences behind single-atom and nanocluster catalytic properties require further exploration for numerous systems. Unraveling the origin of the catalytic differences between nanoclusters and single atoms is complicated by the possibility of dynamic structural rearrangements of the catalytic species and the support under reaction conditions. Transformations between nanoclusters and single atoms often occur[21] as well as the migration of single atoms to defect locations or step edges during a reaction,[22,23] which changes catalytic performance.
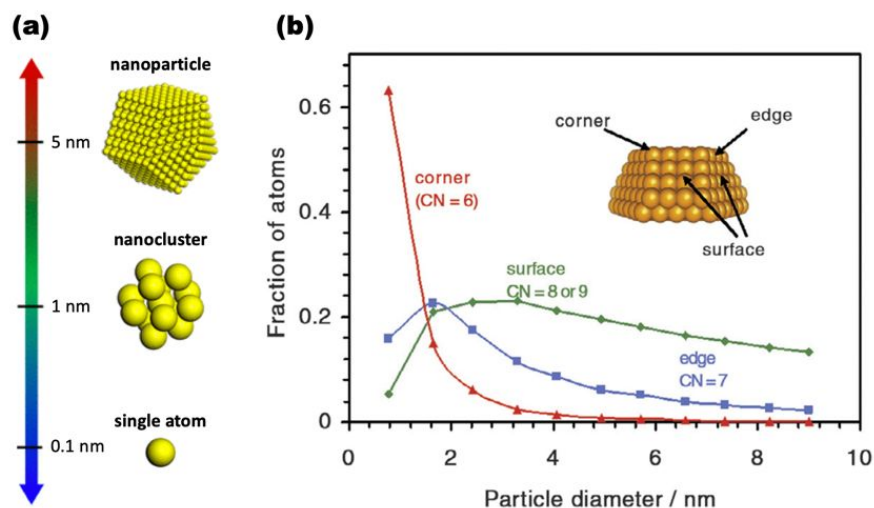


**Fig. 1 (a)** Typical size range of nanoparticles, nanoclusters, and single atoms. Adapted with permission from ref. 18. Copyright 2018 American Chemical Society. **(b)** Relationship between particle diameter and the fraction of corner, edge, and surface (terrace) atoms in a representative supported Au particle shaped as the top half of a truncated octahedron. CN = coordination number. Adapted with permission from ref. 17. Copyright 2007 Elsevier Ltd.

Herein, we survey pertinent topics regarding single-atom and nanocluster precious metal catalysts for thermocatalytic CO oxidation and $CO_2$ reduction reactions. We do not cover electrocatalytic $CO_2$ reduction from single atoms and nanoclusters, but point readers to recent reviews.[24,25] Synthesis approaches to make single atoms and nanoclusters are highlighted, focusing

2

on techniques that produce relatively well-defined catalytic systems for reaction studies. We discuss the thermodynamic driving forces behind single-atom formation from nanoclusters, as well as the role of their spontaneous formation on catalytic performance. Examples of activity, selectivity, and stability differences between nanocluster and single-atom catalysts for CO oxidation and $CO_2$ reduction are emphasized, and we explore how the preferred structure for a catalytic application depends on the material's formulation method and reaction environment. Because single atoms and nanoclusters often change coordination environment in response to reactants, *in situ* characterization under operating conditions and atomistic modeling are critical to understand the structure-property relationships and reaction mechanism. Insights from combined experimental-computational studies will foster rational catalyst synthesis and reaction engineering to maximize the benefits of both nanoclusters and single atoms in tackling challenges related to CO and $CO_2$ conversion.

# 2. Synthesis and Characterization of Single Atoms and Nanoclusters

Synthetic strategies to prepare single atoms and nanoclusters with improved control over the supported metal loading, dispersion, and stability have been expanded over the past decade, from exploiting strong electrostatic adsorption to heat and shockwave methods. Well-defined systems are beneficial to characterize the structure-property relationships of nanoclusters and single-atom catalysts. Therefore, here we review progress in synthesis methods that yield relatively well-defined catalytic species.

## Synthesis of Single-Atom Catalysts

Early generations of single-atom catalysts were made by classic preparation methods using low loadings of supported metals or post-synthetic treatment to selectively remove the supported metal species other than single atoms. The first study to demonstrate single atoms catalyzing both CO oxidation and preferential oxidation of CO in an $H_2$-rich stream was $Pt_1/FeO_x$ made by co-precipitation.[26] Further, a well-defined $Rh_1$ catalyst was made by depositing all $Rh_1$ atoms at the same four-fold hollow site in heteropoly acid supports by co-precipitation.[27] Platinum group metal single-atom species supported on oxides such as $La-Al_2O_3$, $TiO_2$, and $CeO_2$ may also be obtained by dry or wet impregnation, if a low metal loading (< 0.5 wt.%) is chosen to avoid agglomeration of the monomers.[20,28–30] A post-synthetic cyanide leaching approach was applied to $Au/CeO_2$, $Au/FeO_x$, and $Au/TiO_2$ catalysts to remove weakly bound gold nanoparticles from the support surfaces, leaving only strongly bound $Au_1$ single atoms on those support oxides.[31–33]

More recent efforts have focused on developing targeted syntheses of single-atom metal sites on substrates that simplify catalyst preparation procedures and improve the uniformity of the catalytic species. Ion-exchange with a platinum salt precursor was used to prepare a single-site $Pt_1$ catalyst supported on zeolite KLTL.[34] Atomic layer deposition is another frequently employed technique for directly making single-atom catalysts on metal oxide supports with commercially available precursors and programmable operation cycles.[35,36] Strong electrostatic adsorption (SEA) can also produce well-dispersed single-atom catalysts due to targeted interactions between metal precursors and the support via electrostatic adsorption.[37–39] Other single-atom-targeted preparation methods are summarized here with examples provided.

*Thermal, photochemical, and mechanical forces to stimulate metal-support interactions.* Synthetic approaches often use external stimuli such as heat, shockwaves, or UV-Vis electromagnetic radiation to directly make single-atom catalysts. Importantly, single-atom

catalysts synthesized via thermal trapping and high-temperature shockwaves can exhibit excellent sinter resistance because the high synthesis temperatures ensure that stable binding sites are available (e.g., by allowing adatom diffusion to sites that may be thermodynamically favorable but kinetically hindered at low temperatures).[40,41] **Fig. 2a** illustrates how thermal aging at 800 °C of a physical mixture of $Pt/La-Al_2O_3$ and ceria makes thermally stable single-atom $Pt_1/CeO_2$.[40] In this process, volatile $PtO_2$ species leave the Pt nanoparticles on $La-Al_2O_3$ and become trapped by $CeO_2$ as single $Pt_1$ atoms. These trapped $Pt_1$ single atoms were demonstrated to be sinter-resistant and catalytically active under CO oxidation conditions. **Fig. 2b** illustrates how short-duration, high-temperature, shockwaves (1,500–2,000 K, milliseconds) disperse single atoms on supports, followed by quenching to prevent metal vaporization and support deterioration.[41] Instead of applying high temperatures as a source of energy input, single-atom catalysts can be prepared at room temperature by irradiation of UV light. A 1.5 wt.% $Pd_1$ supported on ethylene glycolate (EG)–stabilized $TiO_2$ nanosheets was formed by irradiating UV light on a solution containing $H_2PdCl_4$ and EG-stabilized $TiO_2$ nanosheets. UV-generated EG radicals aided the removal of detrimental chloride ions on Pd and stabilized individual $Pd_1$ atoms.[42] Ball milling is an effective method using mechanical forces to prepare single-atom catalysts by homogeneously mixing different precursors at the atomic level.[43–45] $Pd_1/ZnO$ was made by the ball milling of two acetylacetonate salts ($Pd(acac)_2$ and $Zn(acac)_2$),[46] followed by a calcination at 400 °C in air. This mechanochemical method is straightforward and scales to production ranges of at least 1 kg.
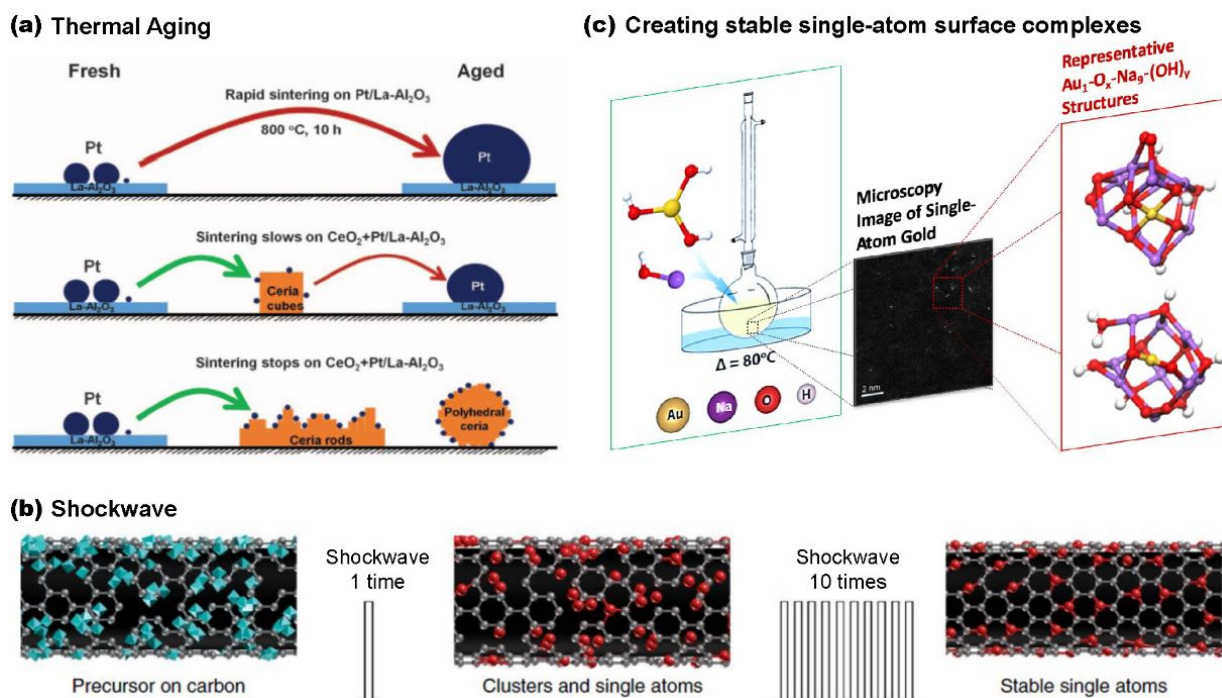


**Fig. 2 Direct synthesis methods for making single-atom catalysts. (a)** Thermal aging of a mixture of $Pt/La-Al_2O_3$ and ceria in air created dispersed $Pt_1/CeO_2$ single atoms that were sinter-resistant at 800 °C. The ceria traps mobile Pt adatoms to prevent sintering. Ceria cubes were less effective than rods or polyhedral ceria for trapping the mobile Pt adatoms. Adapted with permission from ref. 40. Copyright 2016 Association for the Advancement of Science. **(b)** Shockwave method for synthesis and dispersion of single atoms of $Pt_1$, $Ru_1$, or $Co_1$ on carbon (Color legend: gray = C; cyan = metal precursor; red = metal atoms). Adapted with permission from ref. 41. Copyright 2019 Macmillan Publishers Limited, part of Springer Nature. **(c)** Creating stable single-atom gold surface complexes ($Au_1-O_x-Na_9-(OH)_y$) in alkaline solution to

make an $Au_1$–$O_x$–$Na_9$–$(OH)_y$/$TiO_2$ catalyst. Adapted with permission from ref. 47. Copyright 2019 Macmillan Publishers Limited, part of Springer Nature.

*Creating stable single-atom surface complexes from a homogeneous phase.* This strategy involves grafting aqueous-phase inorganometallic/organometallic complexes onto surfaces to produce stable single-atom complexes. Grafting inorganometallic/organometallic complexes from solution provides an additional dimension of controlling single-atom species during catalyst synthesis before utilizing the support properties. A facile and environmentally friendly method was reported by one of the co-authors to prepare a stable inorganometallic gold-oxo complex in the aqueous phase,[47] replacing earlier multi-step sequential preparations.[48,49] As shown in **Fig. 2c**, a liquid suspension of the single-atom gold-oxo complex was prepared by mixing $Au(OH)_3$, NaOH, and water at 80 °C. The liquid suspension was then impregnated onto a $TiO_2$ support and dried to produce an active single-atom gold catalyst ($Au_1$–$O_x$–$Na_9$–$(OH)_y$/$TiO_2$) with up to 1 wt.% gold loading. No further activation steps were required.

Similarly, $Pt_1$/$Fe_2O_3$ was synthesized by using ethanediamine to chelate $Pt^{4+}$ cations, adding this precursor to a suspension of the FeOOH support precursor, then removing the ligands by a rapid thermal treatment from 500 to 600 °C in He.[50] The final coordination chemistry of the $Pt_1$ single atoms was tunable by adjusting the rapid thermal treatment temperature range. In another example, a library of different single-atom catalysts were made by mixing metal cations with 1,10-phenanthroline to form stable metal complexes in aqueous solution,[51] followed by depositing the complexes onto commercial carbon black and pyrolyzing the surface-modified carbon black at 600 °C in Ar. This strategy produced single-atom catalysts up to the kilogram scale with 1.8 wt.% metal loading.

Besides the previously discussed methods, electrochemical treatment may be a promising route to synthesize single-atom catalysts. One proposed strategy is based on the electrochemical potential window,[52] which predicts that aggregated metals on the substrate will leach away by electrochemical oxidation in a certain potential window. In contrast, single atoms or clusters will remain because of their strong bond with the substrate. Grand canonical density functional theory[53] modeling was used to predict the electrochemical potential windows of $Pt_1$, $Pd_1$, and $Ni_1$ supported on N-doped graphene and $Fe_2O_3$, as well as $Pt_3$ and $Ni_3$ anchored on graphdiyne, but experimental validation awaits.

## Synthesis of Supported Nanoclusters

In this section we discuss synthesis methods to produce supported nanoclusters with reasonably controlled size distribution. Many examples exist for developing homogeneous organometallic nanoclusters with precise control at the atomic level.[54–57] However, these advances in chemistry have not yet become closely coupled with the research in heterogeneous catalysis. Reductive treatment and high metal loadings are among the two most common strategies to make supported nanoclusters because these conditions are accessible and create opportunities for supported metal species to agglomerate into clusters on surfaces. Supported nanoclusters are often made by conventional dry or wet impregnation and co-precipitation methods. The nanocluster size is tuned by adjusting the metal loadings and reducing temperatures in the presence of $H_2$.[20,30,58] Other reductive gases such as CO also exhibit a similar result of aggregating the single atoms or nanoclusters to larger particles.[59,60] However, nanoclusters obtained via these strategies often have wide size distributions, suggesting a lack of uniformity of the supported metal sites.

Methods like colloidal synthesis, atomic layer deposition, and strong electrostatic adsorption are common approaches for producing relatively uniform supported nanoclusters.

Preparing nanoclusters from a colloidal solution is a well-established strategy[61–66] in which different sizes of nanoclusters are obtained by adjusting the surfactant type and concentration, the temperature, and the heating duration. In atomic layer deposition, the nanocluster composition and size are tuned by changing the metal precursor and the number of deposition cycles.[67–70] Precise control can even yield dimers.[71] For SEA, the metal loading amount and pH value are crucial for tuning the final size of nanoclusters. Bimetallic nanoparticles can also be made using SEA. A one-pot SEA method incorporating two different metal elements produced a variety of homogeneously alloyed bimetallic nanoclusters.[72] Additional methods to control nanocluster size or enhance their uniformity, dispersion, and stability are summarized here.

*Creating a metal homodimer solution.* The dimer is the smallest nanocluster and is considered a basic unit to interrogate whether a targeted reaction requires the metal catalytic center to be a single-atom species or an ensemble of atoms. The preparation of dinuclear catalysts has been achieved via synthesis of a metal homodimer solution,[73,74] followed by its deposition onto a metal oxide support. Synthesis of Ir dinuclear catalysts on $\alpha$-$Fe_2O_3$ was enabled by a facile photochemical method,[75] as shown in **Fig. 3a**. The $\alpha$-$Fe_2O_3$ support was soaked in the Ir homodimer solution for 10 h, then rinsed with deionized water to form the Ir intermediate, and finally photochemically treated to remove the organic ligands. In another example, Ir dimers complexed with bulky calixarene phosphine ligands have been dispersed on siliceous supports[76] and were found to resist aggregation and deactivation during hydrogenation catalysis. In addition to producing Ir dimers, the homodimer solution method has also produced Rh dimers supported on dehydroxylated MgO using $[Rh_2(C_2H_5)_2]$ complexes.[74]

*Stabilizing metal nanoclusters by molecular frameworks.* Metal nanoclusters often exhibit poor stability under the range of elevated temperatures and pressures present during thermocatalytic $CO_2$ reduction and CO oxidation. Specifically, small nanoclusters can undergo sintering to larger clusters and particles under reaction conditions, as with Pt/CuO clusters that aggregate from an average size of 0.94 nm to 1.38 nm when temperature is increased from 360 K to 500 K.[77] One strategy to address this drawback is to encapsulate nanoclusters inside of porous materials, such as covalent organic frameworks,[78,79] metal organic frameworks,[80–83] and zeolites. Among these, zeolites offer desirable catalytic functions because of their thermal stability, well-controlled pore size distribution, and tunable Lewis and Brønsted acidity.[84] Nanoclusters have been encapsulated into microporous cavities of zeolites to prevent nanocluster sintering.[85,86] Pt clusters (0.2–1.0 nm) were incorporated into the hemi-cages and cages of MCM-22 (MWW-type) zeolite during its transformation from a two-dimensional into a three-dimensional zeolite,[87] as illustrated in **Fig. 3b**. This work synthesized a purely siliceous MWW precursor and used surfactant (hexadecyltrimethylammonium, $CTMA^+OH^-$) to expand the MWW layers to allow incorporation of Pt clusters into the internal channels between individual MWW layers during the swelling process. The organic surfactant was subsequently removed by calcination in air at 540 °C, leaving behind Pt clusters encapsulated by the supercages of the MCM-22 with high stability.

*Catalyst preparation with plasmas.* A plasma is a partially ionized gas consisting of ions, electrons, molecules, excited species, radicals, and photons. The plasma environment allows for catalyst preparation in unique ways compared with traditional thermal methods (e.g., some thermodynamically unfavorable reactions readily occur using plasmas).[88] Because the relative flux of electrons to the nanoclusters is high compared to the flux of positive ions, synthesized nanoparticles are typically negatively charged. The negative charge of the nanoparticles prevents particle sintering and enables the formation of particles smaller than those produced from thermal methods. Employing room-temperature electron reduction with argon glow discharge as an

electron source, stable PtPd core−shell alloy catalysts supported on carbon were made.[89] Much progress has been made in catalyst preparation with plasmas over the last two decades, and we point the reader to a recent review for more information.[88]
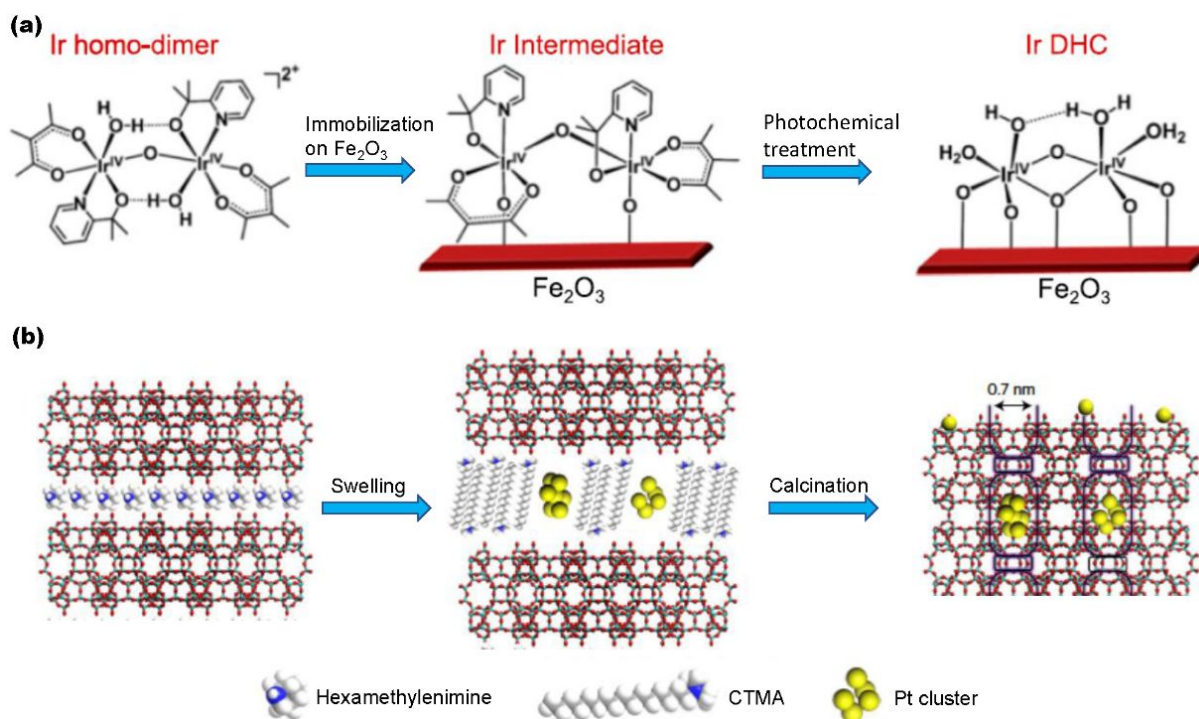


**Fig. 3 Synthesis of nanoclusters with enhanced uniformity, dispersion, or stability. (a)** Synthesis procedure of Ir dinuclear heterogeneous catalysts (DHCs) on $Fe_2O_3$. An Ir homodimer was immobilized on $Fe_2O_3$, followed by the removal of organic ligands via a photochemical treatment. Adapted with permission from ref. 75. Copyright 2018 National Academy of Sciences. **(b)** Encapsulation procedure of Pt clusters (0.2–1.0 nm) into MCM-22 (MWW-type zeolite). The surfactant of hexadecyltrimethylammonium ($CTMA^+OH^-$) was added to expand the MWW layers. Next, the solution of Pt clusters was added during the swelling process of the MCM-22 precursor, which allows the Pt clusters to incorporate into the internal channels between individual MWW layers. The organic agents were removed by calcination to form Pt@MCM-22. Adapted with permission from ref. 87. Copyright 2017 Macmillan Publishers Limited, part of Springer Nature.

## Characterization of Supported Single Atoms and Nanoclusters

Determining the structure and properties of single atoms and nanoclusters requires a combination of microscopy, spectroscopy, probe molecule studies, and modeling techniques. Aberration-corrected high-angle annular dark-field scanning transmission electron microscopy (HAADF-STEM) and X-ray absorption spectroscopy (XAS) are two essential characterization tools to verify the presence of single-atom catalysts.[32,48,90,91] Here, we highlight $Pt_1/FeO_x$ as a case study. If HAADF-STEM images have no visible sign of nanoclusters and instead $Pt_1$ atoms appear dispersed on the support (**Fig. 4a**), and no Pt-Pt bonding is observed in extended x-ray absorption fine structure (EXAFS) spectra (**Fig. 4c**, Sample A), then the sample is likely a single-atom catalyst.[26] The binding environment of the single-atom catalysts can be further interrogated by diffuse reflectance infrared Fourier-transform spectroscopy (DRIFTS), where probe molecules such as CO are used to titrate the supported metal species as a site-specific adsorbate. For typical

$Pt_1$ single-atom catalysts, the full width at half maximum for a single CO adsorption peak in DRIFTS is within 25–30 cm$^{-1}$,[16,28,92–94] indicating a minor amount of heterogeneity attributed to the nuances of local coordination environment. By limiting the Pt loading to less than 0.1 wt.% to achieve exclusively single-atom catalytic sites, the full width at half maximum can be reduced to the range of 6–8 cm$^{-1}$.[38,39] As a contrasting example to the exclusive presence of single atoms in a catalyst, **Fig. 4b** shows a HAADF-STEM image of a mixture of $Pt_1$, Pt rafts with fewer than 10 Pt atoms, and Pt clusters around 1 nm or smaller. For the same sample, Pt-Pt bonding can be observed in EXAFS result (**Fig. 4c**, Sample B, ~2.5 Å). With the evidence provided by the microscopy and X-ray spectra, the authors conclude that sample B is not a single-atom catalyst.
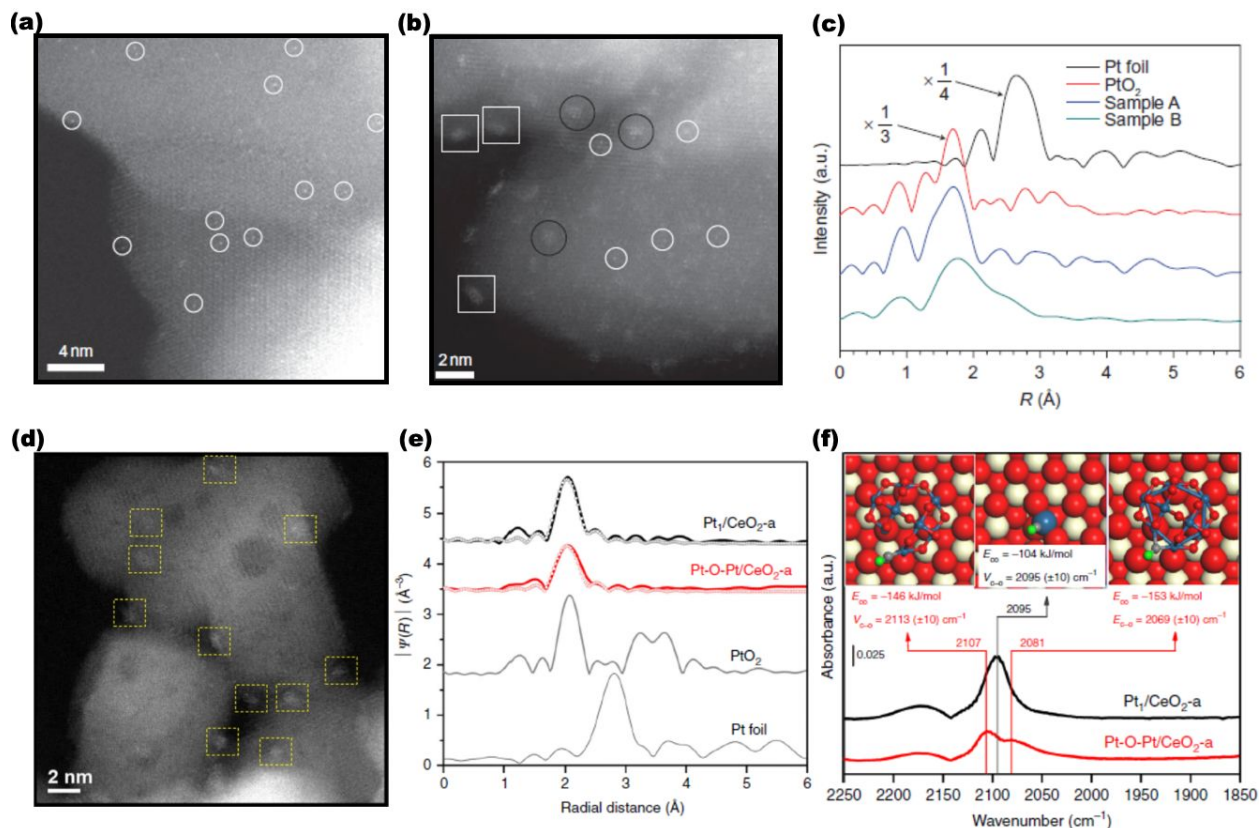


**Fig. 4 Characterization of platinum single-atom and nanocluster catalysts on different supports.** HAADF-STEM images of **(a)** $Pt_1$/FeO$_x$ catalysts and **(b)** a mixture of single-atom (white circles), rafts (black circles), and clusters (white squares) of Pt/FeO$_x$. **(c)** The $k^3$-weighted Fourier transformed EXAFS (Pt L$_3$ edge) related to samples shown in (a) and (b). Sample A is $Pt_1$/FeO$_x$, and B is Pt/FeO$_x$ containing Pt single atoms, rafts, and clusters. Figures (a)–(c) were adapted with permission from ref. 26. Copyright 2011 Macmillan Publishers Limited, part of Springer Nature. **(d)** HAADF-STEM images of Pt-O-Pt/CeO$_2$-a nanocluster with the oxide Pt species around 1 nm in size. **(e)** The $k^2$-weighted Fourier transformed EXAFS (Pt L$_3$ edge, phase corrected) for $Pt_1$/CeO$_2$-a single-atom and Pt-O-Pt/CeO$_2$-a nanocluster catalysts. **(f)** *In situ* DRIFTS under reaction conditions for $Pt_1$/CeO$_2$-a and the Pt-O-Pt/CeO$_2$-a. The CeO$_2$-a are CeO$_2$ hydrothermally aged at 600 °C. CO adsorption energies and vibrational models predicted by DFT are shown inset for $Pt_1$/CeO$_{2-x}$ and $Pt_8O_{13}$/CeO$_2$ model systems. Color legend: beige = Ce; blue = Pt; gray = C; red = O (in CeO$_2$ and $Pt_8O_{13}$); green = O (in CO). Figures d–f were adapted with permission from ref. 16, licensed under a Creative Commons License (http://creativecommons.org/licenses/by/4.0/).

For small metal oxide nanoclusters, such as the Pt-O-Pt/CeO$_2$ sample (~1 nm) in **Fig. 4d**,[16] no Pt-Pt bonding was detected by EXAFS (**Fig. 4e**), and the EXAFS and XPS spectra were similar to that of the Pt$_1$/CeO$_2$ sample. This phenomenon has been observed on Pt/TiO$_2$ and other Pt/CeO$_2$ systems,[20,30] indicating that each Pt atom in the nanocluster is only bonded to O and not to other Pt. The absence of Pt-Pt scattering signals is attributed to experimental signal attenuation at larger radial distances, the potentially one-layer thick structure of these nanoclusters, and the low loading of nanoclusters.[16] In this situation, *in situ* DRIFTS plays a crucial role in distinguishing single-atom and nanocluster catalysts, besides the more visual confirmation from microscopy images (**Fig. 4d**). The data in **Fig. 4f** displays one CO adsorption peak on Pt$_1$/CeO$_2$, whereas two peaks were identified for the Pt-O-Pt/CeO$_2$ nanocluster. The CO adsorption stretching frequencies at 2107 and 2081 cm$^{-1}$ were interpreted as CO chemisorption at the top and bridge sites of the Pt-O-Pt/CeO$_2$ nanocluster based on DFT studies. Grand canonical Monte Carlo simulations identified representative pristine Pt$_8$O$_{14}$ and defected Pt$_8$O$_{13}$ model structures for Pt-O-Pt/CeO$_2$. Sites on defected Pt$_8$O$_{13}$ were predicted to strongly adsorb CO and have vibrational frequencies that matched the experimental DRIFTS, in contrast to the pristine Pt$_8$O$_{14}$. This work highlights the benefit of using a suite of experimental and computational techniques to distinguish single-atom and nanocluster catalysts and understand their local structures at an atomic level.

# 3. Dynamic Structural Changes of Nanoclusters and Single-Atom Catalysts

Understanding the dynamic structural response of nanoclusters and single atoms under reaction conditions is of broad importance because these structural changes can affect their catalytic properties. Under relevant operating conditions for emissions control, the presence of reactants can induce aggregation of single atoms into nanoclusters,[95] or cause disintegration of supported nanoclusters to single atoms.[96–98] Knowledge of the behavior and mechanism of these structural changes in regulating catalytic performance will guide the design of more efficient catalysts for emissions control.

A thermodynamic model was developed to predict the conditions for which reactants induce sintering of smaller particles into larger particles via Ostwald ripening and disintegration of particles into single atoms.[96] This thermodynamic model incorporates how the reaction environment, metal-support interaction, and particle size affects the surface energy of the catalytic species and the Gibb's free energy of particle formation or disintegration. Typically, increasing the reactant partial pressure, lowering the temperature (without kinetically hindering disintegration), and decreasing particle size will increase the thermodynamic driving force for particle disintegration. Although coordinatively unsaturated single atoms on surfaces (adatoms) are often unstable, adsorbates can stabilize the adatoms by complexation. The energy diagram in **Fig. 5a** illustrates how it would be thermodynamically unfavorable for a bare metal atom to detach from a metal nanocluster. In contrast, adsorption of CO lowers the thermodynamic driving force for nanoparticle disintegration to form single-atom complexes. This thermodynamic model predicted that Rh/TiO$_2$(110) nanoclusters were more susceptible to CO-induced disintegration into single atoms than Pd/TiO$_2$(110) and Pt/TiO$_2$(110) nanoclusters because of the highly exothermic formation energy of the stable Rh-dicarbonyl complexes (Rh$_1$(CO)$_2$) compared with Pd- and Pt-carbonyl complexes, consistent with experimental observations.[97] This phenomenon is illustrated in **Fig. 5b** for Rh/TiO$_2$, where the Rh nanocluster disintegrates to form stable Rh$_1$(CO)$_2$ complexes, and these single-atom species can catalyze CO$_2$ reduction to CO with high selectivity.[99]
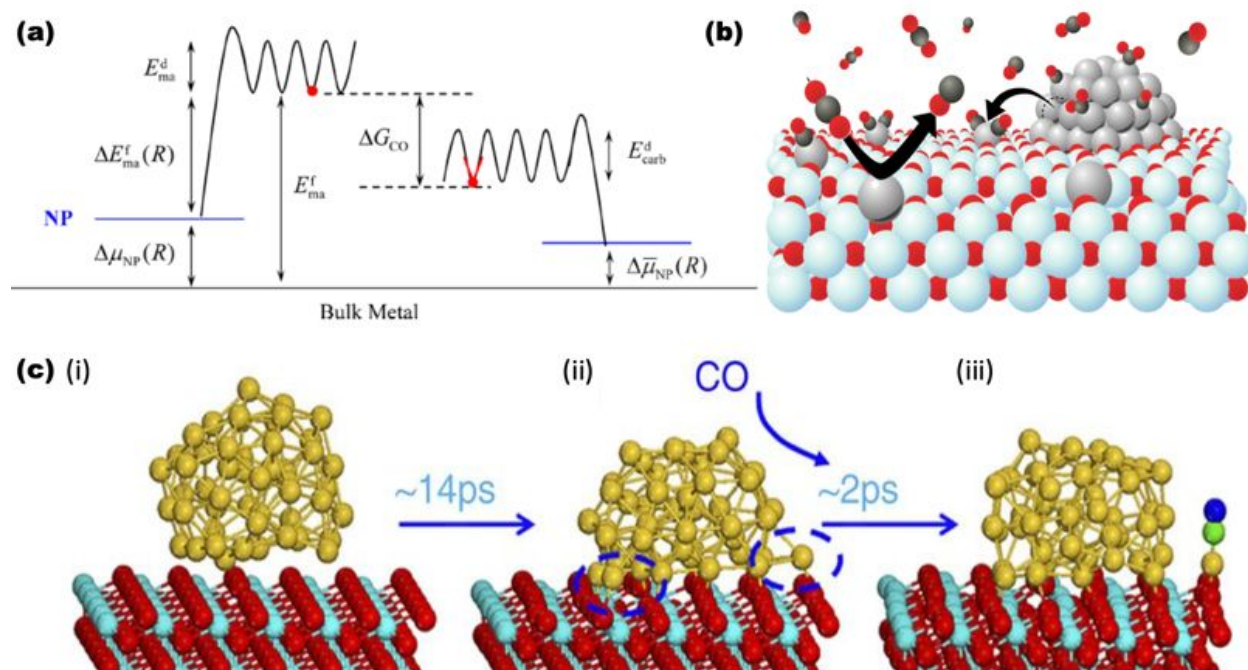
**Fig. 5 Reactant-induced disintegration of nanoclusters into single atoms. (a)** Energy diagram showing how the presence of CO stabilizes a single atom (red dot) by forming a single-atom carbonyl complex with lower formation energy compared with the bare single atom. $\Delta\mu_{NP}(R)$ and $\Delta\bar{\mu}_{NP}(R)$ are the chemical potentials of supported nanoparticles (NPs) without and with reactants present, $E_{ma}^f$ ("ma" refers to a bare metal atom) and $\Delta E_{ma}^f(R)$ are single-atom formation energies on the support with respect to infinite and finite nanoparticle radii ($R$), $\Delta G_{CO}$ is the Gibbs free energy of adsorption of CO on the single atom, and $E_{ma}^d$ and $E_{carb}^d$ ("carb" refers to the carbonyl complex) are the diffusion barriers of single atoms on support. Adapted with permission from ref. 96. Copyright 2013 American Chemical Society. **(b)** Schematic of a Rh nanocluster on $TiO_2$ that is disintegrating in the presence of gaseous reactants (CO, $CO_2$, $H_2$) to form a stable Rh-dicarbonyl complex. The $Rh_1$ species can selectively reduce $CO_2$ to CO and water. Hydrogen and water are not shown. Color legend: light blue = Ti; gray = Rh; red = O; black = C. **(c)** Geometry snapshots from a molecular dynamics simulation of $Au_{50}$/$CeO_2$(111). (i) The initial configuration of $Au_{50}$/$CeO_2$(111); (ii) $Au_{50}$/$CeO_2$(111) after 14 ps of simulation at 700 K, where a low-coordination number gold atom is formed at the metal/support interface (highlighted within the blue circle); (iii) After CO adsorption at the low-coordination gold atom, it separates to form an isolated $Au_1^+$-CO cationic species. Color legend: yellow = Au; teal = Ce; red = O (within ceria); green = C; blue = O (within CO). Adapted with permission from ref. 100, licensed under a Creative Commons License (http://creativecommons.org/licenses/by/4.0/).

Nanocluster disintegration into smaller clusters or single atoms can occur spontaneously under reaction conditions and may either be desired or undesired depending on the application. Volatile single-atom species (e.g., Ni-carbonyl complexes) form from nanoparticles and cause catalyst deactivation.[101,102] In other cases, reactant-induced disintegration has been used to redisperse (and thus reactivate) sintered catalysts for CO oxidation[98,103] and $CO_2$ conversion.[99] A recent study predicted that the dynamic creation of single-atom active sites from Au nanoclusters is essential to catalytic CO oxidation. Single gold cations were simulated by *ab initio* molecular dynamics to break away from the interface of gold nanoparticles on ceria under reaction conditions

to catalyze CO oxidation, **Fig. 5c**.[100] A cationic $Au_1^+$-CO species forms that interacts with the reducible ceria support and consequently has low activation barriers for $CO_2$ formation and desorption. After a catalytic turnover has occurred, the $Au_1$ single atom may recombine with the Au nanoparticle. These simulations suggest the true catalytic species exist transiently under reaction conditions for $Au/CeO_2$. The separation of $Au_1$ single atoms from nanoclusters supported on amorphous carbon was recently confirmed by *in situ* high-resolution TEM and HAADF-TEM[104] while catalyzing $CH_4$ pyrolysis. This finding corroborates the prevalence of nanocluster transformations to single-atom active sites under reaction conditions. The creation of transient adatoms induced by reactant adsorption at the nanocluster interface may be an often overlooked but critical phenomenon in catalytic systems of relevance to emissions control.

The transformation between Pt single atoms and nanoclusters is often reversible, depending on the catalyst-support interactions. This reversible transformation was elucidated in high-silica chabazite zeolite,[58] where Pt oxide nanoclusters (~1 nm) were initially encapsulated within the zeolite. Using *operando* EXAFS and HAADF-STEM characterizations, the Pt nanoclusters were detected to fragment into single atoms in 20% $O_2$/He between 450–650 °C, but the Pt nanoclusters reformed in the presence of 4% $H_2$/He between 150–650 °C. Smaller Pt nanoclusters (0.8–1 nm) were more easily fragmented in an oxidative atmosphere than larger nanoclusters (1–1.5 nm).

Similar oxidative redispersion phenomena were also found on a $Pt/CeO_2$ catalyst,[59] as shown in **Fig. 6a**. *In situ* environmental transmission electron microscopy monitored structural changes of the $Pt/CeO_2$ catalyst induced by oxidative/reductive treatment. Small Pt nanoclusters (< 2 nm) were observed after reduction in $H_2$ at 250 °C, but redispersion into single atoms occurred after oxidizing in $O_2$ at 400 °C. Larger nanoclusters remained intact because they require higher temperatures to redisperse. After another round of reduction in $H_2$ at 250 °C, the Pt nanoclusters reformed from the isolated Pt adatoms. Therefore, the reversible transformation of Pt nanoclusters into single atoms can be achieved by tuning the reducing/oxidizing conditions on ceria. Pd nanoparticles (7.9±0.6 nm) at 0.007 wt.% loading on $Al_2O_3$ were also reported to disintegrate into single atoms after aging in dilute oxygen at 775 °C for one hour.[102]

Besides nanoparticle-to-single-atom transformations induced by oxidative/reductive treatment, there are reports demonstrating nanoparticle dispersion into single atoms or small clusters by reactant-induced ligand effects.[105–107] For example, Rh nanoclusters (1.0–2.5 nm) on $TiO_2$ are stable under $CO_2$:$4H_2$ reaction conditions,[99] but dispersed to $Rh_1$ atoms under $H_2$-lean gas mixture (10$CO_2$:$H_2$), even though $CO_2$ is a relatively weak oxidant. Generally, strongly adsorbing reactants (strong ligands) induce nanoparticle redispersion to single atoms. Nanoparticles of Ru, Rh, Pd, Ag, Ir, and Pt supported on activated carbon (AC) were dispersed to single atoms by reacting with a $CH_3I$ and CO gas mixture.[108] Taking Rh/AC as an example, the dispersion of Rh/AC sample was examined in the presence of a mixture of CO and $CH_3I$ for different durations. Rh nanoclusters remained unchanged at 4–5 nm after two minutes on stream. However, after 15 minutes of treatment, smaller clusters became the predominant species. The *operando* EXAFS results suggest that the Rh-Rh coordination number decreases while the Rh-CO and Rh-I coordination numbers increase with time on stream. These results imply the gradual shrinkage of Rh nanoparticles due to the substitutional coordination by CO and I• free radicals. The atomic dispersion process of Rh nanoparticles by CO and I• ligands was modeled by DFT calculations, **Fig. 6b**. A one-by-one mechanism was postulated in which ligands sequentially attach to a Rh atom and promote separation from the nanocluster. This mechanism was rationalized by the effective atomic number (EAN) and reaction energy for each step. The EAN is defined as the number of electrons around an atomic nucleus, including those from bonded ligands. From the

"EAN rule" based on a filled valence shell, the complex will be most stable with an EAN of 18 (filled $s$, $p$, and $d$ shells),[109] although exceptions to this rule exist for other metallic complexes (e.g., square-planar Pt complexes).[110] By this mechanism, the original Rh nanoparticles (4–5 nm) disperse into $Rh_1$ species as $Rh(CO)_2I_3$(O-AC) and $Rh(CO)I_4$(O-AC) structures. This work clarifies how nanoparticles disintegrate into single atoms through strong interaction with ligands.
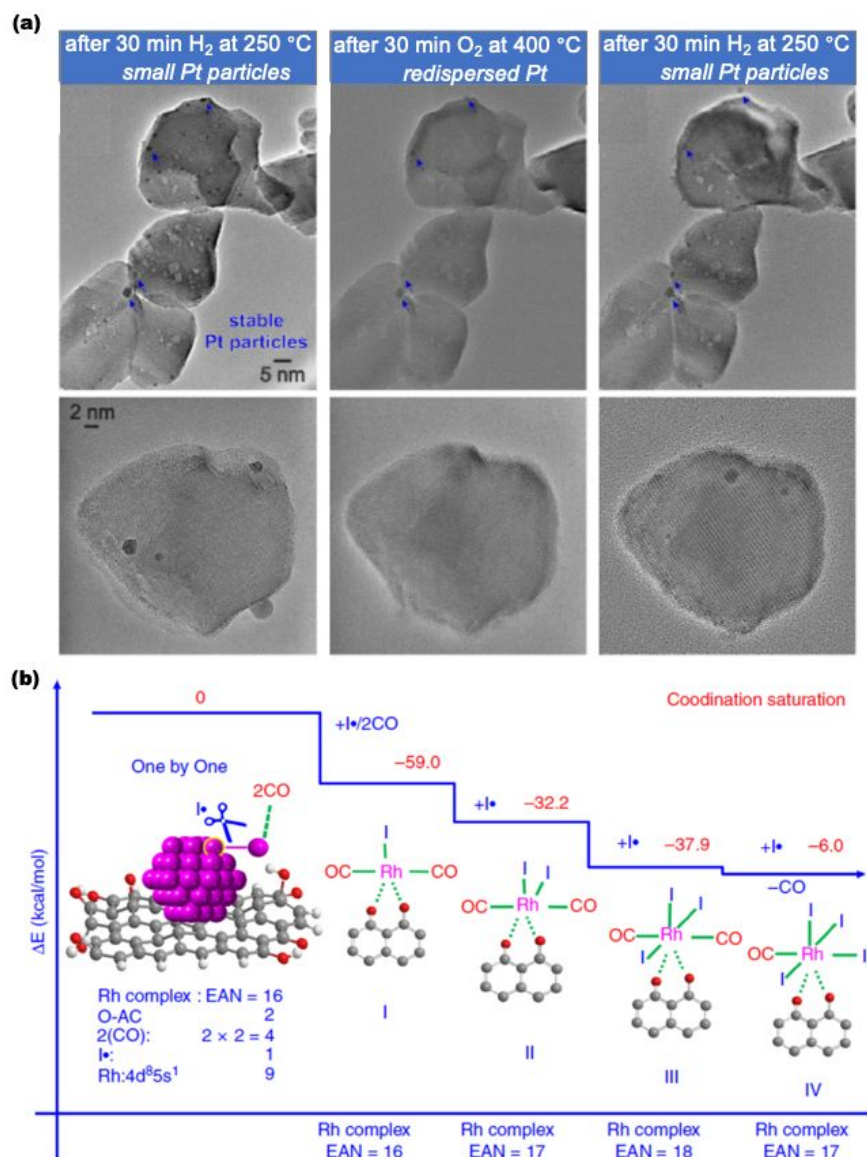


**Fig. 6 Transformation between single atoms and nanoclusters. (a)** Environmental transmission electron microscopy images of Pt/CeO$_2$ captured at three representative areas after reductive treatment by H$_2$ (Pt nanocluster formation), followed by oxidative treatment (Pt redispersion) and by another reductive treatment (Pt nanocluster reformation). Adapted with permission from ref. 59. Copyright 2017 Wiley-VCH Verlag GmbH & Co. KGaA, Weinheim. **(b)** Atomic dispersion model of Rh nanoparticles on activated carbon with CO and I• as ligands via a one-by-one mechanism. The values above every Rh complex model are changes in system energy in kcal/mol. Adapted with permission from ref. 108, licensed under a Creative Commons License (http://creativecommons.org/licenses/by/4.0/).

Although nanoparticle disintegration to single atoms occurs for many systems under reaction conditions, a more pervasive phenomenon is single atoms sintering to larger nanoclusters, resulting in the overall loss of catalytically active metal surfaces. For example, single atoms of $Ni_1$ in $Ni_xMg_{1-x}O$ formed Ni particles up to 10 nm after eight hours of reacting with a $4H_2:1CO_2$ gas mixture at 350 °C and 3 MPa.[111] The reductive reactants and high pressure are driving forces to induce the transformation of single atoms to large nanoclusters. One strategy to improve the sintering resistance of single atoms during CO oxidation and $CO_2$ reduction is to limit diffusion on the support surface through strong metal-support interactions.[40] Uniform $Pt_1/CeO_2$ with low Pt loadings (< 0.1 wt.%) exhibit resistance to reduction and sintering up to 500 °C in 0.05 bar $H_2$,[39] because the $Pt_1$ single atoms adopt thermodynamically stable adsorption sites during the anchoring process at low metal loadings. A DFT study of $Pt_1/CeO_2$, along with a variety of $3d$ (Fe, Co, Ni, Cu), $4d$ (Ru, Rh, Pd, Ag), and $5d$ (Os, Ir, Au) transition metals on ceria, was conducted to examine the sintering resistance of single-atom catalysts.[112] By studying the adsorption energy of different metal cations on a model 79-atom nanocluster of the same metal versus a cuboctahedral $Ce_{40}O_{80}$ nanocluster, the likelihood of sintering for the metal atoms was predicted. All studied cations had stronger binding energy to the ceria cluster than to their own metal clusters, suggesting that single atom dispersion on ceria is preferred over forming metallic particles. However, the resistance to sintering had different magnitudes based on metal identity. Platinum group metals (i.e., Pt, Pd, Ni) and cationic Fe, Os, and Co exhibited high single-atom stability, and therefore a large barrier for sintering, whereas cationic Ag, Au, and Ir were less resistant to agglomeration. The high sintering resistance of the platinum group metals was attributed to the stable square-planar coordination available to $d^8$ metal centers.

# 4. Activity and Selectivity Differences of Single-Atom Catalysts vs. Nanoclusters

## CO Oxidation to $CO_2$

Catalysts often show different activity for CO oxidation depending on the nature of the metal catalytic centers. Whether single atoms or nanoclusters are the more effective catalytic centers for CO oxidation is still debated, although the result likely depends on the target operating conditions and support materials. Several possible mechanisms are proposed for CO oxidation on different catalytic systems, which hinge on the characteristics of metal-support interfaces. The Mars-van Krevelen (MvK) mechanism is often proposed for single atoms and nanoclusters on reducible supports, where a lattice oxygen from the support reacts with bound *CO (on supported metal) to form an O vacancy that is later healed by dissociated $O_2$.[113–115] Other mechanisms include the Langmuir-Hinshelwood (LH) mechanism involving the reaction of adsorbed *O and *CO[116] and the Eley-Rideal (ER) mechanism in which bound *CO reacts directly with gaseous $O_2$.[117] The LH mechanism is often hypothesized for catalysts on irreducible supports that do not form O vacancies easily, whereas the ER mechanism is less commonly proposed due in part to the lower probability for reactive collisions between adsorbed and gaseous species.[5,118]

The study of reaction mechanisms is aided by first-principles calculation approaches such as Density Functional Theory (DFT).[119] DFT modeling enables the relatively rapid prediction of the potential energy diagrams of hypothesized reaction mechanisms. Stable reactant, intermediate, and product states are determined using minima searching algorithms,[120] and transition states connecting elementary steps are found using saddle-point search methods.[121,122] With the potential

energy diagram of the hypothesized reaction mechanism determined (and after including appropriate thermodynamic corrections to obtain free energies), microkinetic models can be constructed to predict apparent activation barriers, degree of rate control, equilibrium coverages, and temperature-dependent reaction rates.[123] To distinguish between the oft-proposed LH and MvK mechanisms for CO oxidation, researchers applied *ab initio* molecular dynamics and microkinetic modeling to predict the kinetics of CO oxidation on $Au/TiO_2$.[124] A mechanism was reported in which $Au_1$ separated from the Au nanocluster and participated in the MvK mechanism, with more favorable kinetics than the LH mechanism. Another study used first-principles microkinetic modeling of $Pt_1/CeO_2$ and found that $Pt_1$ substitution for Ce in the lattice is favorable and promotes nearby O vacancy formation, yielding high CO oxidation activity via the MvK mechanism.[98] Using such microkinetic models allows researchers to effectively bridge the length and timescale gap between electronic-structure theory predictions and experimental measurements.[125]

The difference in activity for CO oxidation by Pt single atoms and nanoclusters on metal oxides has been clarified in recent years. An elegant work created stable $Pt_1$ single atoms on ceria via atom trapping from samples of $Pt/La-Al_2O_3$ physically mixed with different ceria.[40] The different ceria and thermal aging protocols changed the amount of $Pt_1$ single atoms trapped in ceria compared with Pt nanoclusters. These trapped $Pt_1$ catalysts (named as $Pt_1/CeO_2$ below) outperform the aged $Pt/La-Al_2O_3$ nanoparticle (sintered Pt particles as large as 1–2 μm) catalyst for CO oxidation (**Fig. 7a**) below 300 °C. The as-prepared $Pt_1/CeO_2$ did not show any CO conversion at temperatures below 210 °C, and an activation protocol using steam treatment was developed to increase the low-temperature CO oxidation activity of the $Pt_1/CeO_2$. The activation protocol involved flowing 10% $H_2O/Ar$ over $Pt_1/CeO_2$ at 750 °C for 9 hours.[92] **Fig. 7b** illustrates that when the $Pt_1/CeO_2$ is exposed to water at a high temperature of 380 °C, the oxygen vacancies migrate from the bulk to the surface. Subsequently, water molecules heal the oxygen vacancies on the surface and generate neighboring -OH groups with stability up to 767 °C. The surface hydroxyls activate the surface lattice oxygen near the $Pt_1$ catalytic center, which results in a notable activity improvement, **Fig. 7c**. In another effort to activate the $Pt_1/CeO_2$ catalysts, the $Pt_1$ single atoms became nanoclusters with an average size of ~1.6 nm after reduction in CO at 275 °C. Reduced samples with nanoclusters present showed improved CO oxidation activity at low temperatures (**Fig. 7d**), which may be due to the creation of extra surface vacancies on ceria as a result of the single-atom $Pt_1$ migration to form clusters during the reduction step.
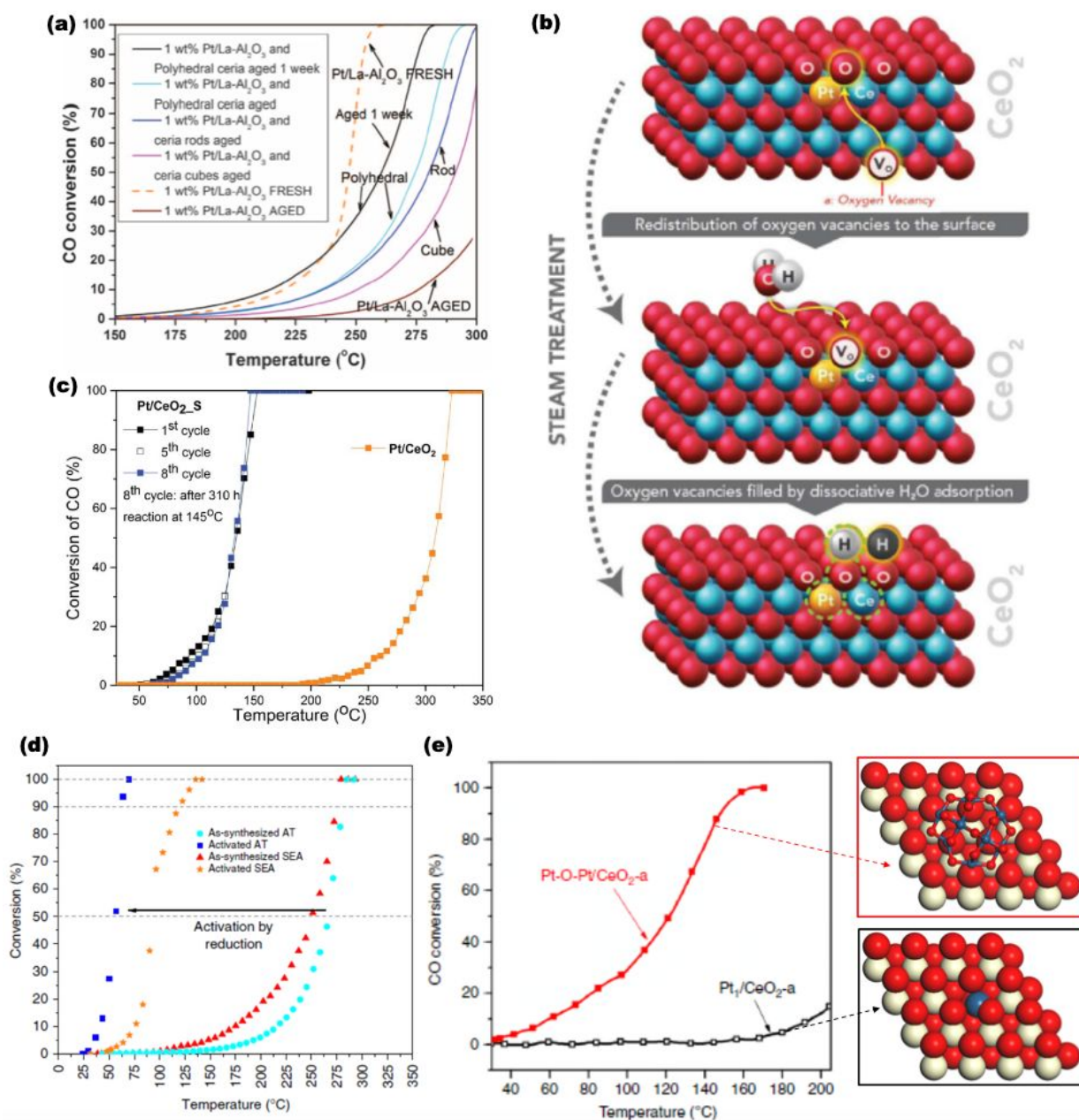
**Fig. 7 Activity comparison of single atoms vs. nanoclusters. (a)** CO oxidation light-off curves for fresh and aged 1 wt.% Pt/La-Al$_2$O$_3$ and 1 wt.% Pt/La-Al$_2$O$_3$ physically mixed with different ceria. All aged Pt/La-Al$_2$O$_3$ samples mixed with ceria contain different amounts of Pt$_1$, whereas the samples not mixed with ceria do not have Pt$_1$ single-atoms. Thermal aging conditions were 800 °C in air. Adapted with permission from ref. 40. Copyright 2016 The American Association for the Advancement of Science. **(b)** Activation process of the Pt$_1$/CeO$_2$ catalyst by steam treatment. The active sites are circled by dash green lines. **(c)** CO oxidation light-off curves of Pt$_1$/CeO$_2$ and the activated Pt$_1$/CeO$_2$. "Pt/CeO$_2$" represents the less active Pt$_1$/CeO$_2$ obtained by thermal aging at 800 °C in air. "Pt/CeO$_2$_S" denotes the activated Pt$_1$/CeO$_2$ by steam treatment. Figures (b) and (c) were adapted with permission from ref. 92. Copyright 2017 The American Association for the Advancement of Science. **(d)** CO oxidation light-off curves for the as-synthesized and activated different 1 wt.% Pt/CeO$_2$ catalysts. "As-synthesized" denotes a single-atom catalyst and "activated" denotes a nanocluster catalyst. Suffixing with AT means atom trapping. Suffixing with SEA denotes strong electronic adsorption. Adapted with permission from ref. 60, licensed under a Creative

Commons License (http://creativecommons.org/licenses/by/4.0/). **(e)** CO oxidation light-off curves for $Pt_1/CeO_2$ and $Pt-O-Pt/CeO_2$. DFT-optimized structures of representative single-atom Pt in the $Pt_1/CeO_2$ sample and $Pt_8O_{14}$ in the $Pt-O-Pt/CeO_2$ sample are shown. Color legend: beige = Ce; red = O (large in ceria, small in cluster); blue = Pt. Adapted with permission from ref. 16, licensed under a Creative Commons License (http://creativecommons.org/licenses/by/4.0/).

We used a facile redox method to transform isolated $Pt_1$ atoms on $CeO_2$ into nanoclusters around 1 nm in size with the catalytic unit of a Pt-O-Pt ensemble (denoted as $Pt-O-Pt/CeO_2$).[16] Each Pt atom in the $Pt-O-Pt/CeO_2$ nanocluster was 100–1000 times more active than the $Pt_1/CeO_2$ in catalyzing CO oxidation in the range of 80–150 °C under oxygen-rich conditions. As shown in **Fig. 7e**, the isolated $Pt_1$ atoms substituted the Ce atoms rather than anchor on the $CeO_2(111)$ surface. DFT modeling and grand canonical Monte Carlo simulations identified $Pt_8O_{14}$ as a representative structure for $Pt-O-Pt/CeO_2$. Using first-principles microkinetic modeling and comparing with experimental reaction orders, a reaction mechanism was proposed based on the $Pt_8O_{14}$ structure in which oxygen atom migration at the Pt-O-Pt ensemble is the rate-determining step. The lattice oxygen of $CeO_2$ was found to be uninvolved in the low-temperature catalytic cycle. The results highlight that proper arrangement of multiple Pt atoms can lead to a large enhancement in catalytic activity relative to their single atom constituents, even without relying on the presence of O vacancies in the ceria. Of course, further investigation into strategies to stabilize these active but transient nanoclusters is needed. Recent work reported that epitaxial growth of Pt clusters on $LaFeO_3/MgAl_2O_4$ was restricted to the size range of 1–2 nm because of strong metal-support interactions.[126] The authors found these small Pt clusters with a near two-dimensional morphology can survive even after five redox cycles at 800 °C, without significant sintering and loss of catalytic activity for CO oxidation.

Catalytic activity for CO oxidation is often sensitive to the precise morphology of the nanocluster catalyst. For example, the activities of ~1 nm mass-selected Pt nanoclusters supported on $Al_2O_3/NiAl(110)$ and $TiO_2(110)$ were studied as a function of cluster thickness.[127] The mass-selected Pt nanoclusters were characterized based on cluster diameter and height using scanning tunneling microscopy and categorized by the number of atoms and number of cluster layers (one-layer cluster (< 19 atoms), two-layer cluster (19–30 atoms), and three-layer cluster (> 30 atoms)). The charge characteristics of each cluster's atoms were probed using IR spectroscopy in the presence of CO. The data showed distinct peaks for adsorbed CO on cationic Pt and neutral Pt. These findings purport that Pt atoms at the metal-support interface were cationic, whereas atoms away from the interface were neutral. For either support, the ratio of neutral to cationic Pt atoms in two-layer clusters was higher than that of the one-layer and three-layer clusters. The two-layer cluster also had higher CO oxidation activity than clusters of one or three layers, attributed to its higher ratio of neutral Pt atoms. This finding was rationalized by the preference for electronegative $O_2$ to bind to neutral Pt sites, allowing for $O_2$ to dissociate and react readily with bound CO on two-layer clusters. DFT calculations corroborate the experimental nanocluster characterizations by modeling the cluster structure for each size using a bond additivity model. One-layer clusters were most stable up to 18 atoms, which transitioned to two layers between 19–26 atoms and three layers above 27 atoms, which agreed with experimental characterization by scanning tunneling microscopy. Comparing the experimentally determined ratio of neutral to cationic Pt with the simulated result, the same trend of two-layer clusters having the highest Pt neutral to cationic ratio was found. In another example, single Au atoms and nanoclusters with two or three dimensions were supported on ZnO.[128] The two-dimensional Au layer clusters displayed better intrinsic CO oxidation activity than single atoms and the three-dimensional Au species. In contrast to the Pt

16

cluster example, the increased activity of 2D clusters was hypothesized to originate from the higher ratio of interfacial cationic $Au^{\delta+}$ to neutral Au.

## CO$_2$ Reduction to CO and CH$_4$

Due to environmental concerns, $CO_2$ reduction has been a broad and topical research area in heterogeneous catalysis. A collection of recent reviews and perspectives on $CO_2$ reduction highlight diverse topics such as photocatalysis, electrocatalysis, and the role of metal-support interfaces in thermocatalytic reactions.[129–133] We differentiate our discussion by highlighting the different aspects of single atoms vs. nanoclusters for $CO_2$ reduction to CO and methane. Generally, the $CO_2$ reduction reaction mechanism depends heavily on the structural properties of catalysts. Additionally, the desorption behavior of CO is a key factor in determining the selectivity during $CO_2$ reduction. If the desorption of CO is favorable, reverse water gas shift reaction (RWGS) is the dominant reaction. Otherwise, further hydrogenation occurs to products such as methane or formic acid.[134–136] For many metal catalysts supported on metal oxides, single metal atoms tend to promote CO production via RWGS, whereas metal clusters promote $CH_4$ production via catalytic methanation. Herein, we will focus on the formation of CO and $CH_4$ products because of their versatility as feedstocks, but some systems often favor other products, including formic acid or methanol.

Varying the ratio of clusters to single atoms causes a dramatic change in selectivity for $CO_2$ reduction by metals supported on both irreducible and reducible metal oxides. For example, low Ru loadings (0.1 wt.%) resulted in $Ru_1$ single atoms on $Al_2O_3$[137] and CO formation with ~85% selectivity from $CO_2$ reduction. After $CO_2$ reduction at 350 °C for 16 h, the formation of Ru nanoclusters (2−10 nm) was observed, and this structural change was accompanied by a concurrent decrease in CO formation rate and an increase in $CH_4$ yield. Extracted apparent activation energies revealed that formate or bicarbonate are more likely intermediates than CO in the formation of $CH_4$.[138] This evidence suggests a shift in reaction pathway as the catalyst structure changed from single atoms to nanoclusters.

Multiple studies support the observation of a different reaction pathway between single atoms and nanoclusters for $CO_2$ reduction. For example, a 2 wt.% Rh was deposited on $TiO_2$ by impregnation to form Rh nanoclusters between 1.0–1.5 nm.[99] The Rh/$TiO_2$ sample underwent a HCl/$H_2O_2$-based leaching process to selectively remove nanoclusters, leaving behind mostly $Rh_1$ single atoms on the support. CO DRIFTS with known site-specific extinction coefficients was employed to quantify the fraction of various Rh sites. When $CO_2$ reduction was conducted on the fresh and leached samples, the $CH_4$ production rate on every exposed Rh site declined by 88% after leaching, and the CO production rate decreased by 28%. These results demonstrate that the $Rh_1$ single atoms favor RWGS, whereas nanoclusters (1.0–2.5 nm) favor methanation. In another study, Ir nanoparticles were deposited on ceria to study how nanocluster size and coordination environment affect $CO_2$ reduction selectivity. The sizes of Ir clusters were adjusted to 2.2, 1.6, and 1.0 nm by varying Ir loadings from 20, 15, and 5 wt.%, respectively.[139] The Ir coordination environment, which can be tuned by the particle size, seemed to determine the selectivity in $CO_2$ hydrogenation. The Ir-O bond favors CO production, whereas the metallic Ir-Ir bond facilitates methanation. Ir/$TiO_2$ single atoms and clusters for $CO_2$ reduction were also studied through DFT modeling (**Fig. 8a**).[135] Compared with the step edges of an Ir surface, the $Ir_1$ catalyst had a 2.45 eV higher activation barrier for CO dissociation. The work concludes that the $Ir_1$ catalyst prevents carbonyl dissociation and favors CO desorption. In contrast, Ir clusters were more capable of dissociating CO and further hydrogenating the intermediate to $CH_4$. More recent work similarly

confirmed the RWGS reaction occurring on $Pt_1/CeO_2$, while methanation was more favored on $Pt/CeO_2$ nanoclusters.[140]

Shifts in catalyst selectivity to make either CO or $CH_4$ from $CO_2$ reduction by single atoms and nanoclusters have been reported. The $CO_2$ reduction selectivity of Ru nanoclusters supported on $CeO_2$, $Al_2O_3$, and $TiO_2$ were examined.[8] The work synthesized Ru nanoclusters with different sizes, but here we discuss the Ru nanoclusters of 2.6±0.3 nm as an example. Low-temperature $H_2$ reduction pretreatment of the nanoclusters at 230 °C was performed because metallic Ru can dissociate $H_2$ easily, making the catalyst a suitable material for methanation with high activity and selectivity. No change in the cluster size occurred from the reductive pretreatment. However, the reaction product distribution changed if an oxidative treatment was added at 230 °C before the $H_2$ reduction. The oxidative treatment switches the catalyst selectivity from methanation to RWGS, regardless of whether the support is $Al_2O_3$, $TiO_2$, or $CeO_2$. As shown in **Fig. 8b**, the oxidation-reduction treated samples are denoted as "OX-LTR" (oxidation–low temperature reduction) and "OX-HTR" (oxidation–high temperature reduction), both of which show higher CO selectivity than the "LTR" (low temperature reduction) sample. *In situ* and *ex situ* XAS revealed that oxidative treatment induced the redispersion of Ru nanoclusters into atomically dispersed $RuO_x$ species, thus rationalizing the shift in catalytic function. In another example, a $Ni_1$ single-atom catalyst, $Ni_xMg_{1-x}O$, was made via a solid solution approach,[111] and 1–10% $Mg^{2+}$ was substituted by $Ni^{2+}$ inside the MgO structure. As shown in **Fig. 8c**, single atoms of Ni are active and stable for producing CO from $CO_2$ reduction even at 300 °C. At 350 °C, an onset of methanation can be observed, where formation of Ni nanoclusters up to 10 nm occurs. When the reaction temperature returned to 300 from 350 °C, the product distribution and the conversion rate of $CO_2$ differ from the trend observed for the as-prepared $Ni_1$ catalyst, indicative of irreversible sintering of single atoms to nanoclusters.

For the highlighted examples (e.g., $Ru/Al_2O_3$, $Rh/TiO_2$, $Pt/CeO_2$, $Ru/CeO_2$, and $Ni_xMg_{1-x}O$), there is a general selectivity tradeoff between RWGS and methanation based on the supported metal species. Typically, the RWGS is preferred when single atoms are the majority species, whereas the catalytic reaction proceeds through the methanation pathway when nanoclusters are the dominant species. This selectivity difference aligns with the observation that single atoms typically bind CO weaker than nanoclusters, which allows CO to desorb from single atoms more readily than nanoclusters. Nanoclusters offer bridge sites that bind CO more strongly by way of two atoms, and this ensemble effect is not present with single atoms.[141] Additionally, the difference in ability of single atoms and nanoclusters to dissociate hydrogen may also contribute to the selectivity differences.[99,142,143] Nonetheless, exceptions to this selectivity trend do exist. Recently, a $Co/\gamma-Mo_2N$ nanocluster catalyst, with an average of four Co atoms in each Co cluster, exhibited high CO selectivity of > 98%.[144] The Co precursor was impregnated in the pre-synthesized $\gamma-Mo_2N$, and the Co atoms assembled into nanoclusters after activation in a $N_2-H_2$ mixture at 863 K for two hours. This work found that the Co-N linkage is the primary chemical bond anchoring the Co nanoclusters to the support. Charge transfer from Co to $Mo_2N$ inhibits the full dissociation of $CO_2$, thereby preventing the generation of the C or $CH_x$ fragments that are necessary for methane formation. This work highlights the key role of the support material in regulating the reaction pathways, in addition to the chemistry of the supported metal structures.
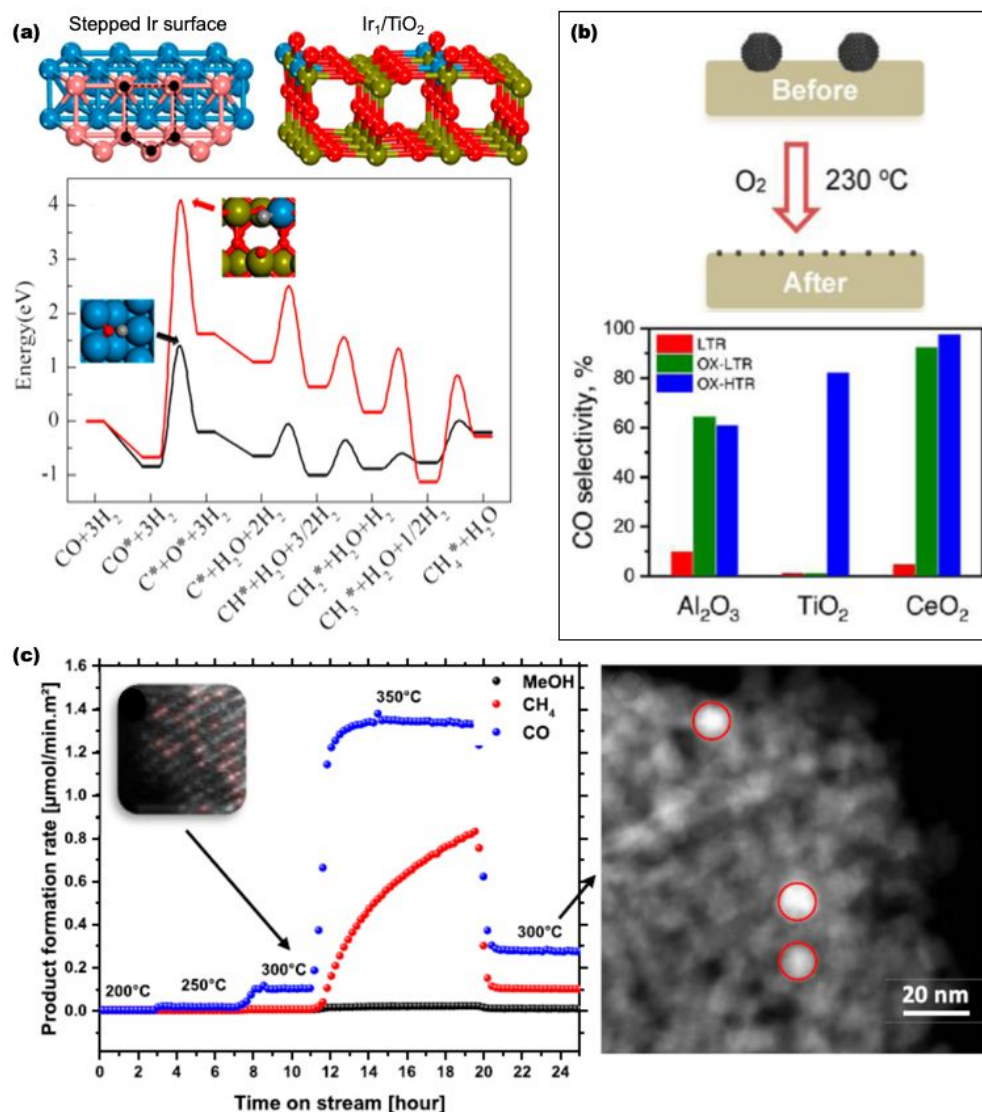
**Fig. 8 CO$_2$ reduction activity and selectivity comparison of single-atom and nanocluster catalysts. (a)** Comparison of CO conversion to CH$_4$ for stepped Ir surface (black line) and Ir$_1$ supported on rutile TiO$_2$(110) (red line). Structures of stepped Ir surface and Ir$_1$/TiO$_2$. Color legend: yellow = Ti; red = O; blue = Ir; pink = Ir step atoms. Ir$_1$/TiO$_2$ shows a larger activation barrier for CO dissociation than the stepped Ir surface and prefers CO desorption. Adapted with permission from ref. 135. Copyright 2018 American Chemical Society. **(b)** Size-dependent CO selectivity on Ru/Al$_2$O$_3$, Ru/TiO$_2$, and Ru/CeO$_2$ for CO$_2$ reduction reaction. The top image illustrates Ru nanoparticle dispersion to single atoms after oxidative treatment at 230 °C. The bottom image shows CO selectivity for Ru species on Al$_2$O$_3$, TiO$_2$, and CeO$_2$ supports. LTR: low temperature reduction at 230 °C; OX-LTR: oxidation at 230 °C and low temperature reduction at 230 °C; and OX-HTR: oxidation at 230 °C and high temperature reduction at 530 °C. Adapted with permission from ref. 8. Copyright 2018 American Chemical Society. **(c)** Product formation rate of CO, CH$_4$, or methanol by Ni$_x$Mg$_{1-x}$O with Ni content of 10 wt.% at 30 bar with 4H$_2$:1CO$_2$ gas mixture at different temperatures. The inset HAADF-STEM image represents the sample after testing at 300 °C, and the right HAADF-STEM image represents the sample after testing at 350 °C. Ni nanoclusters of 10 nm are marked in red circles. Adapted with permission from ref. 111. Copyright 2019 American Chemical Society.

## Influence of Coordination Environment Changes on Catalytic Performance

Understanding how the coordination environment of single atoms and nanoclusters change under reaction conditions and their effect on catalytic performance is important for catalyst design and mechanistic understanding. Advances in *in situ* spectroscopy under reaction conditions have led to many insights into how the structure of heterogeneous catalysts on stream affects their activity, selectivity, and stability. *In situ* EXAFS enables detailed studies of the nanocluster and single-atom coordination environment in response to reactants.[145] For example, $PtO_x$ clusters on ceria nanowires were studied under CO oxidation conditions.[30] EXAFS fits showed the coordination number of Pt-O increased from 1.7 to 2.3 under reaction conditions over 350 min (**Fig. 9a**) and the corresponding $CO_2$ production rate decreased (**Fig. 9b**), showing a high Pt-O coordination number is detrimental to CO oxidation. The weaker CO binding strength to the more highly coordinated Pt-O sites may explain the decrease in the $CO_2$ production rate.

*In situ* spectroscopy under reaction conditions combined with atomistic modeling has provided insight into how single atoms change their coordination environment in response to reactants. A recent study elucidated that a $Pt_1/TiO_2$ catalyst,[146] containing ~0.5 Pt atoms per $TiO_2$ particle, can adopt different local coordination environments and oxidation states that depend on the reaction environment. *In situ* XAS revealed the diverse coordination environments of single-atom $Pt_1$ after oxidation, mild reduction, and harsh reduction pretreatments. DFT calculations corroborated the different $Pt_1$ sites existing at step edges and substituting for lattice Ti by reproducing the CO binding energies, vibrational frequencies, and experimental Pt-O bond lengths. Varying the pretreatment conditions led to distinct coordination environments for $Pt_1$, and in turn, distinct initial CO oxidation activities. However, the $Pt_1$ in these varied pretreated samples eventually all exhibited similar catalytic performance after reaching similar oxidation states and local coordination environments under CO oxidation conditions.

The coordination changes for nine different $Rh_1/TiO_2(110)$ structures under $H_2$, CO, and RWGS conditions were studied in a joint experimental-computational study.[21] $Rh_1$ single atoms were modeled by *ab initio* thermodynamics (**Fig. 9c**) to understand whether they substitute for Ti (**Fig. 9d**) or bind onto the $TiO_2(110)$ surface (**Fig. 9e**). By varying the oxygen chemical potential ($\mu(O)$) of the environment surrounding the $Rh_1/TiO_2$ system, the favored arrangement of the Rh atom placement and $TiO_x$ stoichiometry can be influenced, thereby affecting the catalytic reactivity. Following the line of the lowest chemical potential in **Fig. 9c**, the preferred structure passes through three possible configurations. Under oxygen-rich conditions (high $\mu(O)$), $Rh_1$ prefers to substitute at the six-fold coordinated Ti site on a clean $TiO_2$ surface. As oxygen chemical potential decreases, oxygen vacancies form near $Rh_1$, and as oxygen chemical potential decreases further, the Rh atom instead prefers to adsorb above a three-fold coordinated oxygen vacancy. The experimental observations from CO infrared spectroscopy and scanning transmission electron microscopy confirmed the DFT-predicted response of Rh single atoms under $O_2$ gas (high $\mu(O)$) and $H_2$ and CO gas (low $\mu(O)$).
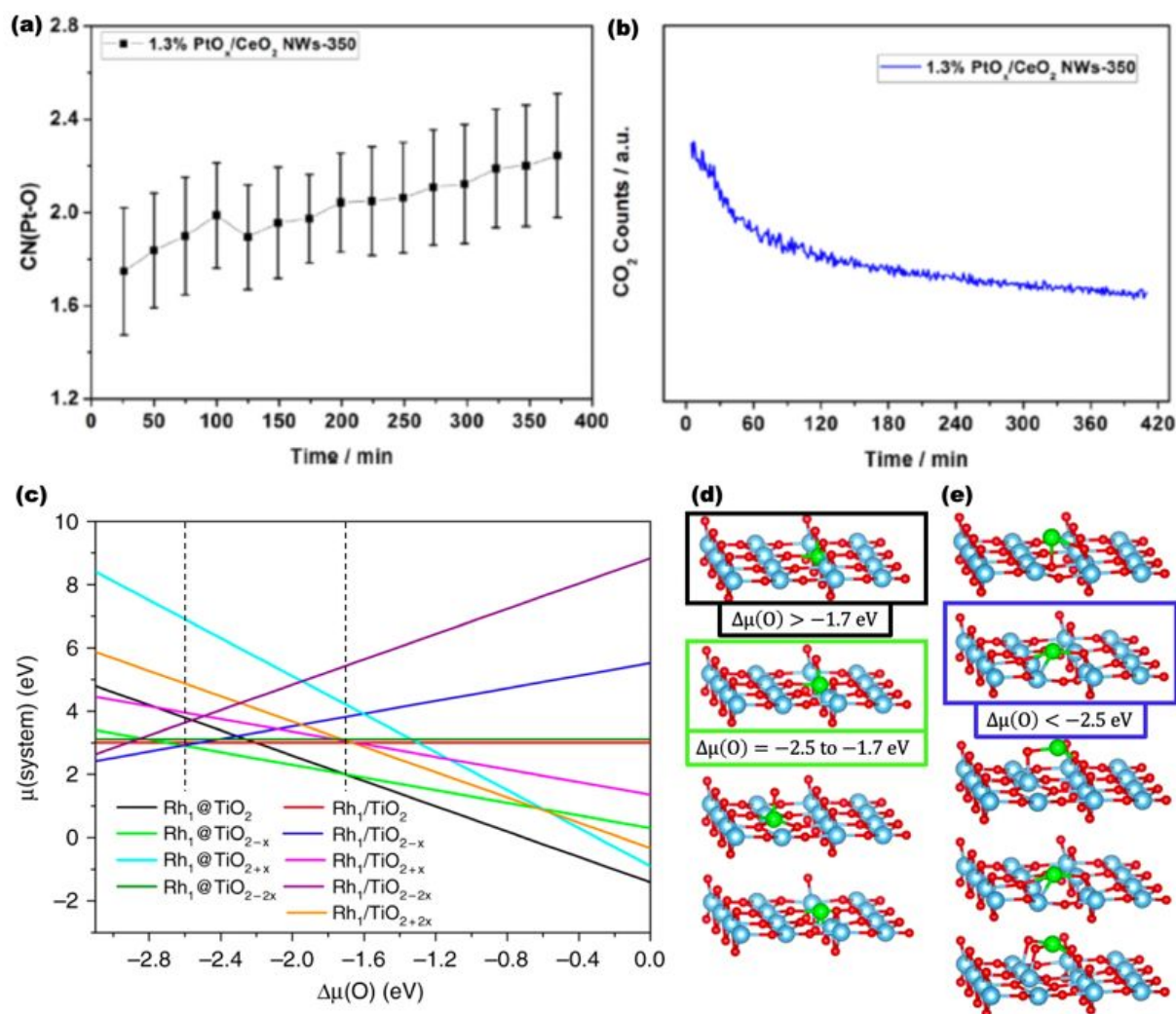
**Fig. 9 Coordination environment changes in response to reactants and the effect on catalytic performance. (a)** *In situ* EXAFS spectra fitting results of the Pt−O coordination numbers (CN(Pt-O)) for 1.3% wt.% $PtO_x/CeO_2$ nanowires with the fitting error along the reaction time. **(b)** $CO_2$ evolution on the same $PtO_x/CeO_2$ nanowires during *in situ* analysis obtained from mass spectrometry. Figures (a) and (b) were adapted with permission from ref. 30. Copyright 2015 American Chemical Society. **(c)** Stability trends of different $Rh_1$ single atom binding locations on rutile $TiO_2(110)$ at substitutional (@) and supported (/) sites relative to oxygen chemical potential ($\Delta\mu(O)$). The study includes stoichiometric $TiO_2$, oxygen-deficient $TiO_{2-x}$, and excess oxygen $TiO_{2+x}$. The optimal structures for **(d)** substitutional and **(e)** supported $Rh_1$ single atoms on the rutile $TiO_2(110)$ surfaces. Here the $Rh_1$ species adopt different preferred sites based on changing oxygen chemical potential, with $Rh_1@TiO_2$ (black) preferred under oxygen-rich conditions ($\Delta\mu(O) > -1.7$ eV), $Rh_1@TiO_{2-x}$ (light green) under moderate conditions ($-2.5$ eV $< \Delta\mu(O) < -1.7$ eV), and $Rh_1/TiO_{2-x}$ (blue) under oxygen-poor conditions ($\Delta\mu(O) < -2.5$ eV). Color legend: red = O; blue = Ti; green = Rh. Figures (c)–(e) were adapted with permission from ref. 21, licensed under a Creative Commons License (http://creativecommons.org/licenses/by/4.0/).

Besides the coordination changes in response to reactants for the traditional CO oxidation and $CO_2$ reduction, the correlation between the single-atom coordination structure and catalytic performance has also been elucidated for other reactions. The activity of $Pt_1/Fe_2O_3$ as a function of coordination structure was clarified for chemoselective hydrogenation of 3-nitrostyrene to 3-

vinylaniline.[50] In this work, a series of $Pt_1/Fe_2O_3$ samples with gradually decreasing Pt-O coordination numbers were obtained by increasing the rapid thermal treatment temperature. Samples with a smaller Pt-O coordination or a lower oxidation state of the $Pt_1$ species correlated with higher catalytic activity for chemoselective hydrogenation. This finding demonstrates that the coordination environment has a major influence on the catalytic performance of single-atom catalysts.

Coordination environment also often has a large effect on nanocluster catalytic activity as well. Generally, supported nanoclusters adopt a variety of sizes and shapes that are difficult to know *a priori*, particularly in the presence of adsorbates.[147] Consequently, a major challenge for modeling nanoclusters is finding model systems with realistic sizes, shapes, and surface compositions under reaction conditions. Many algorithms have been developed to model the diversity of nanocluster structures such as genetic algorithms,[148,149] basin hopping,[150] and grand canonical Monte Carlo.[151,152] However, modeling supported nanoclusters under realistic conditions is computationally demanding and requires much human effort. Nevertheless, there have been many advances in understanding the fluxionality of nanoclusters under reaction conditions via modeling. By fluxionality, we mean the dynamic nanocluster structural rearrangements triggered by adsorbates and reactions.[147] *Ab initio* molecular dynamics simulations have shown substantial isomerization of $Pt_{13}$ clusters while dissociating methane at 400 K, far beyond what is observed thermally at 700 K.[153] Further modeling suggests that small Pt clusters can also break linear scaling relationships by way of their fluxionality compared with bulk metal or larger nanoparticles. Another instance of small cluster isomerization with beneficial catalytic effects is the dynamic restructuring of palladium-copper tetrahydride anions ($PdCuH_4^-$) for $CO_2$ reduction.[155] By a joint experimental-theoretical approach, these bimetallic hydride clusters were shown to convert $CO_2$ into formate and formic acid through a series of metastable cluster configurations. The lowest energy isomer had a 2.38 eV activation barrier for formate desorption, but a metastable isomer allowed for a more favorable overall reaction path, with two smaller barriers of 0.95 and 0.80 eV. These findings demonstrate the importance of studying multiple possible cluster structures as active sites, including metastable structures. On-going research is focusing on using machine learning to accelerate the structure search of catalysts,[156–158] which may benefit future studies of supported nanoclusters under reaction conditions and how their coordination environment influences catalytic performance.

# 5. Outlook

Catalytic performance is often sensitive to the morphology and composition of the catalytic center, which is exemplified by the distinct catalytic behaviors of single-atoms and nanoclusters. For the environmentally relevant reactions of CO oxidation and $CO_2$ reduction, substantial effort has gone into understanding and expanding the capabilities of heterogeneous catalysts for efficient and selective conversion while minimizing precious metal use. The choice of support, active metal, dispersion, and reaction conditions all play crucial roles in determining the preferred product and achieving favorable kinetics. In this Minireview, we have discussed multiple approaches for synthesizing single-atom and nanocluster catalysts with high specificity and explored how nanoclusters and single atoms differ in activity and selectivity for CO and $CO_2$ conversion. We highlighted experimental evidence and atomistic models that demonstrate the common dynamic structural changes between nanoclusters and single-atom catalysts under reaction conditions, as well as how these coordination environment changes affect the catalytic performance. For CO

oxidation, single atoms have been observed to form under reaction conditions from supported nanoclusters and provide alternative active sites that often proceed through a Mars-van Krevelen mechanism. Research has shown that ~1 nm Pt nanoclusters can be more active for low-temperature CO oxidation (< 150 °C) than single atoms, but that Pt single-atoms become more active at higher temperatures. For thermocatalytic $CO_2$ reduction by $H_2$, the general trend often holds that single atoms on both reducible and irreducible supports promote the formation of CO, whereas nanoclusters produce $CH_4$. This selectivity difference is hypothesized to arise from the weak adsorption of CO on single atoms compared with nanoclusters and the lack of nearby metal sites to dissociate $H_2$. Still, the $CO_2$ reduction mechanisms differ between systems, and the precise reaction pathways are still being investigated on both single atoms and nanoclusters.

Developing improved catalytic processes for CO and $CO_2$ conversion will require advances in controlling and understanding the nanocluster and single atom structures under reaction conditions. Advanced synthesis approaches are needed to develop catalysts with (i) uniform size to clarify structure-performance relationships for target reactions and (ii) improved stability for practical applications. Theoretical modeling approaches continue to improve for studying nanocluster and single atom stability under reaction conditions, but the field of predictive synthesis of single atoms and nanoclusters to guide experiments is still developing. State-of-the-art modeling techniques such as *ab initio* molecular dynamics and grand canonical Monte Carlo allow for a wide range of exploration of catalyst surfaces and morphologies exposed to reactants, but these techniques are computationally demanding. Accelerating computational catalysis modeling by machine learning promises to increase the pace of innovation and discovery. Likewise, machine learning and data science techniques can be further exploited to advance the analysis of the rich output from kinetic and spectroscopic experiments, which will help uncover hidden patterns between catalyst structure, reactive intermediates, and overall performance. Finally, although much of the recent progress for CO oxidation and $CO_2$ conversion has focused on thermo- and electro-catalysis, there is room for advances in emerging fields such as nonthermal plasma-assisted catalysis by nanoclusters and single atoms. New approaches for experimentation and modeling of plasma-surface interactions are actively being devised, and advances in this area may prove fruitful for CO and $CO_2$ conversion applications.

## Conflicts of interest

There are no conflicts to declare.

## Acknowledgements

## References

1    H. S. Taylor, *Proc. R. Soc. Lond. Ser. Contain. Pap. Math. Phys. Character*, 1925, **108**, 105–111.
2    J. N. Armor, *Catal. Today*, 2011, **163**, 3–9.
3    R. J. Farrauto, M. Deeba and S. Alerasool, *Nat. Catal.*, 2019, **2**, 603–613.

4    A. Beniya and S. Higashi, *Nat. Catal.*, 2019, **2**, 590–602.

5    M. A. van Spronsen, J. W. M. Frenken and I. M. N. Groot, *Chem. Soc. Rev.*, 2017, **46**, 4347–4374.

6    J. A. Rodriguez, D. C. Grinter, Z. Liu, R. M. Palomino and S. D. Senanayake, *Chem. Soc. Rev.*, 2017, **46**, 1824–1841.

7    M. D. Porosoff, B. Yan and J. G. Chen, *Energy Environ. Sci.*, 2016, **9**, 62–73.

8    A. Aitbekova, L. Wu, C. J. Wrasman, A. Boubnov, A. S. Hoffman, E. D. Goodman, S. R. Bare and M. Cargnello, *J. Am. Chem. Soc.*, 2018, **140**, 13736–13745.

9    X. Su, X.-F. Yang, Y. Huang, B. Liu and T. Zhang, *Acc. Chem. Res.*, 2019, **52**, 656–664.

10   R. B. Anderson, *Fischer-Tropsch synthesis*, Academic Press, Inc., New York, NY, 1984.

11   D. Iribarren, A. Susmozas and J. Dufour, *Renew. Energy*, 2013, **59**, 229–236.

12   F. Jiao, J. Li, X. Pan, J. Xiao, H. Li, H. Ma, M. Wei, Y. Pan, Z. Zhou, M. Li, S. Miao, J. Li, Y. Zhu, D. Xiao, T. He, J. Yang, F. Qi, Q. Fu and X. Bao, *Science*, 2016, **351**, 1065–1068.

13   M. Jouny, G. S. Hutchings and F. Jiao, *Nat. Catal.*, 2019, **2**, 1062–1070.

14   P. Mehta, P. Barboun, D. B. Go, J. C. Hicks and W. F. Schneider, *ACS Energy Lett.*, 2019, **4**, 1115–1133.

15   H. Jeong, G. Lee, B.-S. Kim, J. Bae, J. W. Han and H. Lee, *J. Am. Chem. Soc.*, 2018, **140**, 9558–9565.

16   H. Wang, J.-X. Liu, L. F. Allard, S. Lee, J. Liu, H. Li, J. Wang, J. Wang, S. H. Oh, W. Li, M. Flytzani-Stephanopoulos, M. Shen, B. R. Goldsmith and M. Yang, *Nat. Commun.*, 2019, **10**, 3808.

17   B. Hvolbæk, T. V. W. Janssens, B. S. Clausen, H. Falsig, C. H. Christensen and J. K. Nørskov, *Nano Today*, 2007, **2**, 14–18.

18   L. Liu and A. Corma, *Chem. Rev.*, 2018, **118**, 4981–5079.

19   E. Fernández, L. Liu, M. Boronat, R. Arenal, P. Concepcion and A. Corma, *ACS Catal.*, 2019, **9**, 11530–11541.

20   L. Liu, D. M. Meira, R. Arenal, P. Concepcion, A. V. Puga and A. Corma, *ACS Catal.*, 2019, **9**, 10626–10639.

21   Y. Tang, C. Asokan, M. Xu, G. W. Graham, X. Pan, P. Christopher, J. Li and P. Sautet, *Nat. Commun.*, 2019, **10**, 4488.

22   S. Tosoni and G. Pacchioni, *Surf. Sci.*, 2017, **664**, 87–94.

23   Q. Wan, F. Wei, Y. Wang, F. Wang, L. Zhou, S. Lin, D. Xie and H. Guo, *Nanoscale*, 2018, **10**, 17893–17901.

24   S. Nitopi, E. Bertheussen, S. B. Scott, X. Liu, A. K. Engstfeld, S. Horch, B. Seger, I. E. L. Stephens, K. Chan, C. Hahn, J. K. Nørskov, T. F. Jaramillo and I. Chorkendorff, *Chem. Rev.*, 2019, **119**, 7610–7672.

25   F. Lü, H. Bao, Y. Mi, Y. Liu, J. Sun, X. Peng, Y. Qiu, L. Zhuo, X. Liu and J. Luo, *Sustain. Energy Fuels*, 2020, **4**, 1012–1028.

26   B. Qiao, A. Wang, X. Yang, L. F. Allard, Z. Jiang, Y. Cui, J. Liu, J. Li and T. Zhang, *Nat. Chem.*, 2011, **3**, 634–641.

27   M. J. Hülsey, B. Zhang, Z. Ma, H. Asakura, D. A. Do, W. Chen, T. Tanaka, P. Zhang, Z. Wu and N. Yan, *Nat. Commun.*, 2019, **10**, 1330.

28   H. Wang, J. Dong, L. F. Allard, S. Lee, S. Oh, J. Wang, W. Li, M. Shen and M. Yang, *Appl. Catal. B Environ.*, 2019, **244**, 327–339.

29    E. J. Peterson, A. T. DeLaRiva, S. Lin, R. S. Johnson, H. Guo, J. T. Miller, J. H. Kwak, C. H. F. Peden, B. Kiefer, L. F. Allard, F. H. Ribeiro and A. K. Datye, *Nat. Commun.*, 2014, **5**, 4885.

30    J. Ke, W. Zhu, Y. Jiang, R. Si, Y.-J. Wang, S.-C. Li, C. Jin, H. Liu, W.-G. Song, C.-H. Yan and Y.-W. Zhang, *ACS Catal.*, 2015, **5**, 5164–5173.

31    Q. Fu, H. Saltsburg and M. Flytzani-Stephanopoulos, *Science*, 2003, **301**, 935–938.

32    M. Yang, L. F. Allard and M. Flytzani-Stephanopoulos, *J Am Chem Soc*, 2013, **135**, 3768–3771.

33    L. F. Allard, A. Borisevich, W. Deng, R. Si, M. Flytzani-Stephanopoulos and S. H. Overbury, *J. Electron Microsc. (Tokyo)*, 2009, **58**, 199–212.

34    J. D. Kistler, N. Chotigkrai, P. Xu, B. Enderle, P. Praserthdam, C.-Y. Chen, N. D. Browning and B. C. Gates, *Angew. Chem.*, 2014, **126**, 9050–9053.

35    C. Wang, X.-K. Gu, H. Yan, Y. Lin, J. Li, D. Liu, W.-X. Li and J. Lu, *ACS Catal.*, 2017, **7**, 887–891.

36    J. A. Singh, N. Yang and S. F. Bent, *Annu. Rev. Chem. Biomol. Eng.*, 2017, **8**, 41–62.

37    J. R. Regalbuto, Ed., in *Catalyst preparation: Science and Engineering*, Taylor & Francis, Boca Raton, 2007.

38    L. DeRita, S. Dai, K. Lopez-Zepeda, N. Pham, G. W. Graham, X. Pan and P. Christopher, *J Am Chem Soc*, 2017, **139**, 14150–14165.

39    J. Resasco, L. DeRita, S. Dai, J. P. Chada, M. Xu, X. Yan, J. Finzel, S. Hanukovich, A. S. Hoffman, G. W. Graham, S. R. Bare, X. Pan and P. Christopher, *J. Am. Chem. Soc.*, 2019, **142**, 169–184.

40    J. Jones, H. Xiong, A. T. DeLaRiva, E. J. Peterson, H. Pham, S. R. Challa, G. Qi, S. Oh, M. H. Wiebenga, X. I. Pereira Hernandez, Y. Wang and A. K. Datye, *Science*, 2016, **353**, 150–154.

41    Y. Yao, Z. Huang, P. Xie, L. Wu, L. Ma, T. Li, Z. Pang, M. Jiao, Z. Liang, J. Gao, Y. He, D. J. Kline, M. R. Zachariah, C. Wang, J. Lu, T. Wu, T. Li, C. Wang, R. Shahbazian-Yassar and L. Hu, *Nat. Nanotechnol.*, 2019, **14**, 851–857.

42    P. Liu, Y. Zhao, R. Qin, S. Mo, G. Chen, L. Gu, D. M. Chevrier, P. Zhang, Q. Guo, D. Zang, B. Wu, G. Fu and N. Zheng, *Science*, 2016, **352**, 797–800.

43    W. Zhan, S. Yang, P. Zhang, Y. Guo, G. Lu, M. F. Chisholm and S. Dai, *Chem. Mater.*, 2017, **29**, 7323–7329.

44    K. Cheng, B. Gu, X. Liu, J. Kang, Q. Zhang and Y. Wang, *Angew. Chem. Int. Ed.*, 2016, **55**, 4725–4728.

45    H. Schreyer, R. Eckert, S. Immohr, J. de Bellis, M. Felderhoff and F. Schüth, *Angew. Chem. Int. Ed.*, 2019, **58**, 11262–11265.

46    X. He, Y. Deng, Y. Zhang, Q. He, D. Xiao, M. Peng, Y. Zhao, H. Zhang, R. Luo, T. Gan, H. Ji and D. Ma, *Cell Rep. Phys. Sci.*, 2020, **1**, 100004.

47    S. Cao, M. Yang, A. O. Elnabawy, A. Trimpalis, S. Li, C. Wang, F. Göltl, Z. Chen, J. Liu, J. Shan, M. Li, T. Haas, K. W. Chapman, S. Lee, L. F. Allard, M. Mavrikakis and M. Flytzani-Stephanopoulos, *Nat. Chem.*, 2019, **11**, 1098–1105.

48    M. Yang, J. Liu, S. Lee, B. Zugic, J. Huang, L. F. Allard and M. Flytzani-Stephanopoulos, *J. Am. Chem. Soc.*, 2015, **137**, 3470–3473.

49    M. Yang, S. Li, Y. Wang, J. A. Herron, Y. Xu, L. F. Allard, S. Lee, J. Huang, M. Mavrikakis and M. Flytzani-Stephanopoulos, *Science*, 2014, **346**, 1498–1501.

50    Y. Ren, Y. Tang, L. Zhang, X. Liu, L. Li, S. Miao, D. S. Su, A. Wang, J. Li and T. Zhang, *Nat. Commun.*, 2019, **10**, 4500.

51    H. Yang, L. Shang, Q. Zhang, R. Shi, G. I. N. Waterhouse, L. Gu and T. Zhang, *Nat. Commun.*, 2019, **10**, 4585.

52    J.-C. Liu, H. Xiao and J. Li, *J. Am. Chem. Soc.*, , DOI:10.1021/jacs.9b06808.

53    R. Sundararaman, W. A. Goddard and T. A. Arias, *J. Chem. Phys.*, 2017, **146**, 114104.

54    J. Oliver-Meseguer, J. R. Cabrero-Antonino, I. Domínguez, A. Leyva-Pérez and A. Corma, *Science*, 2012, **338**, 1452–1455.

55    M. K. Samantaray, E. Pump, A. Bendjeriou-Sedjerari, V. D'Elia, J. D. A. Pelletier, M. Guidotti, R. Psaro and J.-M. Basset, *Chem. Soc. Rev.*, 2018, **47**, 8403–8437.

56    *Coord. Chem. Rev.*, 2017, **353**, 278–294.

57    T.-A. D. Nguyen, Z. R. Jones, B. R. Goldsmith, W. R. Buratto, G. Wu, S. L. Scott and T. W. Hayton, *J. Am. Chem. Soc.*, 2015, **137**, 13319–13324.

58    M. Moliner, J. E. Gabay, C. E. Kliewer, R. T. Carr, J. Guzman, G. L. Casty, P. Serna and A. Corma, *J. Am. Chem. Soc.*, 2016, **138**, 15743–15750.

59    A. M. Gänzler, M. Casapu, P. Vernoux, S. Loridant, F. J. Cadete Santos Aires, T. Epicier, B. Betz, R. Hoyer and J.-D. Grunwaldt, *Angew. Chem. Int. Ed.*, 2017, **56**, 13078–13082.

60    X. I. Pereira-Hernández, A. DeLaRiva, V. Muravev, D. Kunwar, H. Xiong, B. Sudduth, M. Engelhard, L. Kovarik, E. J. M. Hensen, Y. Wang and A. K. Datye, *Nat. Commun.*, 2019, **10**, 1358.

61    J. Zhang, Y. Li, X. Zhang and B. Yang, *Adv. Mater.*, 2010, **22**, 4249–4269.

62    F. Li, D. P. Josephson and A. Stein, *Angew. Chem.-Int. Ed.*, 2011, **50**, 360–388.

63    J. M. Romo-Herrera, R. A. Alvarez-Puebla and L. M. Liz-Marzan, *Nanoscale*, 2011, **3**, 1304–1315.

64    S. E. Lohse and C. J. Murphy, *J. Am. Chem. Soc.*, 2012, **134**, 15607–15620.

65    T. Bollhorst, K. Rezwan and M. Maas, *Chem. Soc. Rev.*, 2017, **46**, 2091–2126.

66    M. Vanden Brink, M. A. Peck, K. L. More and J. D. Hoefelmeyer, *J. Phys. Chem. C*, 2008, **112**, 12122–12126.

67    S. T. Christensen, H. Feng, J. L. Libera, N. Guo, J. T. Miller, P. C. Stair and J. W. Elam, *Nano Lett.*, 2010, **10**, 3047–3051.

68    J. Lu, K.-B. Low, Y. Lei, J. A. Libera, A. Nicholls, P. C. Stair and J. W. Elam, *Nat. Commun.*, 2014, **5**, 3264.

69    J. Dendooven, R. K. Ramachandran, E. Solano, M. Kurttepeli, L. Geerts, G. Heremans, J. Rongé, M. M. Minjauw, T. Dobbelaere, K. Devloo-Casier, J. A. Martens, A. Vantomme, S. Bals, G. Portale, A. Coati and C. Detavernier, *Nat. Commun.*, 2017, **8**, 1074.

70    Z. Gao and Y. Qin, *Acc. Chem. Res.*, 2017, **50**, 2309–2316.

71    H. Yan, Y. Lin, H. Wu, W. Zhang, Z. Sun, H. Cheng, W. Liu, C. Wang, J. Li, X. Huang, T. Yao, J. Yang, S. Wei and J. Lu, *Nat. Commun.*, 2017, **8**, 1070.

72    A. Wong, Q. Liu, S. Griffin, A. Nicholls and J. R. Regalbuto, *Science*, 2017, **358**, 1427–1430.

73    P. Serna and B. C. Gates, *Acc. Chem. Res.*, 2014, **47**, 2612–2620.

74    D. Yardimci, P. Serna and B. C. Gates, *Chem. - Eur. J.*, 2013, **19**, 1235–1245.

75    Y. Zhao, K. R. Yang, Z. Wang, X. Yan, S. Cao, Y. Ye, Q. Dong, X. Zhang, J. E. Thorne, L. Jin, K. L. Materna, A. Trimpalis, H. Bai, S. C. Fakra, X. Zhong, P. Wang, X. Pan, J. Guo, M. Flytzani-Stephanopoulos, G. W. Brudvig, V. S. Batista and D. Wang, *Proc. Natl. Acad. Sci.*, 2018, **115**, 2902–2907.

76    C. Schöttle, E. Guan, A. Okrut, N. A. Grosso-Giordano, A. Palermo, A. Solovyov, B. C. Gates and A. Katz, *J. Am. Chem. Soc.*, 2019, **141**, 4010–4015.

77    X. Zhou, W. Yang, Q. Chen, Z. Geng, X. Shao, J. Li, Y. Wang, D. Dai, W. Chen, G. Xu, X. Yang and K. Wu, *J. Phys. Chem. C*, 2016, **120**, 1709–1715.

78    X. Shi, Y. Yao, Y. Xu, K. Liu, G. Zhu, L. Chi and G. Lu, *ACS Appl. Mater. Interfaces*, 2017, **9**, 7481–7488.

79    Y. Deng, Z. Zhang, P. Du, X. Ning, Y. Wang, D. Zhang, J. Liu, S. Zhang and X. Lu, *Angew. Chem. Int. Ed.*, 2020, **59**, 6082–6089.

80    S. Li, J. Pan, X. Wu, Y. Fu, Q. Xiao, F. Zhang and W. Zhu, *Appl. Organomet. Chem.*, 2019, **33**, e5233.

81    Z. Wang, R. Chen, Y. Xiong, K. Cepe, J. Schneider, R. Zboril, C.-S. Lee and A. L. Rogach, *Part. Part. Syst. Charact.*, 2017, **34**, 1700029.

82    R. Wei, C. A. Gaggioli, G. Li, T. Islamoglu, Z. Zhang, P. Yu, O. K. Farha, C. J. Cramer, L. Gagliardi, D. Yang and B. C. Gates, *Chem. Mater.*, 2019, **31**, 1655–1663.

83    D. Yang and B. C. Gates, *ACS Catal.*, 2019, **9**, 1779–1798.

84    S. Li, A. Zheng, Y. Su, H. Zhang, L. Chen, J. Yang, C. Ye and F. Deng, *J. Am. Chem. Soc.*, 2007, **129**, 11161–11171.

85    M. Choi, Z. Wu and E. Iglesia, *J. Am. Chem. Soc.*, 2010, **132**, 9129–9137.

86    S. Goel, Z. Wu, S. I. Zones and E. Iglesia, *J. Am. Chem. Soc.*, 2012, **134**, 17688–17695.

87    L. Liu, U. Díaz, R. Arenal, G. Agostini, P. Concepción and A. Corma, *Nat. Mater.*, 2017, **16**, 132–138.

88    Z. Wang, Y. Zhang, E. C. Neyts, X. Cao, X. Zhang, B. W.-L. Jang and C. Liu, *ACS Catal.*, 2018, **8**, 2093–2110.

89    W. Wang, Z. Wang, J. Wang, C. Zhong and C. Liu, *Adv. Sci.*, , DOI:10.1002/advs.201600486.

90    M. Flytzani-Stephanopoulos and B. C. Gates, *Annu. Rev. Chem. Biomol. Eng.*, 2012, **3**, 545–574.

91    X.-F. Yang, A. Wang, B. Qiao, J. Li, J. Liu and T. Zhang, *Acc. Chem. Res.*, 2013, **46**, 1740–1748.

92    L. Nie, D. Mei, H. Xiong, B. Peng, Z. Ren, X. I. P. Hernandez, A. DeLaRiva, M. Wang, M. H. Engelhard, L. Kovarik, A. K. Datye and Y. Wang, *Science*, 2017, **358**, 1419–1423.

93    K. Ding, A. Gulec, A. M. Johnson, N. M. Schweitzer, G. D. Stucky, L. D. Marks and P. C. Stair, *Science*, 2015, **350**, 189–192.

94    Z. Zhang, Y. Zhu, H. Asakura, B. Zhang, J. Zhang, M. Zhou, Y. Han, T. Tanaka, A. Wang, T. Zhang and N. Yan, *Nat. Commun.*, 2017, **8**, 16100.

95    Y.-Q. Su, J.-X. Liu, I. A. W. Filot and E. J. M. Hensen, *Chem. Mater.*, 2017, **29**, 9456–9462.

96    R. Ouyang, J.-X. Liu and W.-X. Li, *J. Am. Chem. Soc.*, 2013, **135**, 1760–1771.

97    B. R. Goldsmith, E. D. Sanderson, R. Ouyang and W.-X. Li, *J. Phys. Chem. C*, 2014, **118**, 9588–9597.

98    Y.-Q. Su, Y. Wang, J.-X. Liu, I. A. W. Filot, K. Alexopoulos, L. Zhang, V. Muravev, B. Zijlstra, D. G. Vlachos and E. J. M. Hensen, *ACS Catal.*, 2019, **9**, 3289–3297.

99    J. C. Matsubu, V. N. Yang and P. Christopher, *J. Am. Chem. Soc.*, 2015, **137**, 3076–3084.

100   Y.-G. Wang, D. Mei, V.-A. Glezakou, J. Li and R. Rousseau, *Nat. Commun.*, 2015, **6**, 6511.

101   M. Agnelli, M. Kolb and C. Mirodatos, *J. Catal.*, 1994, **148**, 9–21.

102 E. D. Goodman, A. C. Johnston-Peck, E. M. Dietze, C. J. Wrasman, A. S. Hoffman, F. Abild-Pedersen, S. R. Bare, P. N. Plessow and M. Cargnello, *Nat. Catal.*, 2019, **2**, 748–755.

103 L. Liu, D. N. Zakharov, R. Arenal, P. Concepcion, E. A. Stach and A. Corma, *Nat. Commun.*, 2018, **9**, 574.

104 W. Xi, K. Wang, Y. Shen, M. Ge, Z. Deng, Y. Zhao, Q. Cao, Y. Ding, G. Hu and J. Luo, *Nat. Commun.*, 2020, **11**, 1919.

105 A. Goguet, C. Hardacre, I. Harvey, K. Narasimharao, Y. Saih and J. Sa, *J. Am. Chem. Soc.*, 2009, **131**, 6973–6975.

106 J. Sá, A. Goguet, S. F. R. Taylor, R. Tiruvalam, C. J. Kiely, M. Nachtegaal, G. J. Hutchings and C. Hardacre, *Angew. Chem.*, 2011, **123**, 9074–9078.

107 J. Sá, S. F. R. Taylor, H. Daly, A. Goguet, R. Tiruvalam, Q. He, C. J. Kiely, G. J. Hutchings and C. Hardacre, *ACS Catal.*, 2012, **2**, 552–560.

108 S. Feng, X. Song, Y. Liu, X. Lin, L. Yan, S. Liu, W. Dong, X. Yang, Z. Jiang and Y. Ding, *Nat. Commun.*, 2019, **10**, 5281.

109 *J. Soc. Chem. Ind.*, 1928, **47**, 226–227.

110 P. R. Mitchell and R. V. Parish, *J. Chem. Educ.*, 1969, **46**, 811.

111 M.-M. Millet, G. Algara-Siller, S. Wrabetz, A. Mazheika, F. Girgsdies, D. Teschner, F. Seitz, A. Tarasov, S. V. Levchenko, R. Schlögl and E. Frei, *J. Am. Chem. Soc.*, 2019, **141**, 2451–2461.

112 A. Figueroba, G. Kovács, A. Bruix and K. M. Neyman, *Catal. Sci. Technol.*, 2016, **6**, 6806–6813.

113 P. Mars and D. W. van Krevelen, *Chem. Eng. Sci.*, 1954, **3**, 41–59.

114 J.-X. Liu, Y. Su, I. A. W. Filot and E. J. M. Hensen, *J. Am. Chem. Soc.*, 2018, **140**, 4580–4587.

115 H. Y. Kim and G. Henkelman, *J. Phys. Chem. Lett.*, 2013, **4**, 216–221.

116 C. Jia, W. Zhong, M. Deng and J. Jiang, *J. Chem. Phys.*, 2018, **148**, 124701.

117 Y. Lu, J. Wang, L. Yu, L. Kovarik, X. Zhang, A. S. Hoffman, A. Gallo, S. R. Bare, D. Sokaras, T. Kroll, V. Dagle, H. Xin and A. M. Karim, *Nat. Catal.*, 2019, **2**, 149–156.

118 H. Xu, C.-Q. Xu, D. Cheng and J. Li, *Catal. Sci. Technol.*, 2017, **7**, 5860–5871.

119 J. K. Nørskov, F. Studt, F. Abild-Pedersen and T. Bligaard, *Fundamental concepts in heterogeneous catalysis*, Wiley, Hoboken, New Jersey, 2014.

120 H. B. Schlegel, *J. Comput. Chem.*, 2003, **24**, 1514–1527.

121 G. Henkelman, B. P. Uberuaga and H. Jónsson, *J. Chem. Phys.*, 2000, **113**, 9901–9904.

122 B. Peters, A. Heyden, A. T. Bell and A. Chakraborty, *J. Chem. Phys.*, 2004, **120**, 7877–7886.

123 I. A. W. Filot, R. A. van Santen and E. J. M. Hensen, *Angew. Chem. Int. Ed.*, 2014, **53**, 12746–12750.

124 Y.-G. Wang, D. C. Cantu, M.-S. Lee, J. Li, V.-A. Glezakou and R. Rousseau, *J. Am. Chem. Soc.*, 2016, **138**, 10467–10476.

125 A. Bruix, J. T. Margraf, M. Andersen and K. Reuter, *Nat. Catal.*, 2019, **2**, 659–670.

126 X. Mao, A. C. Foucher, T. Montini, E. A. Stach, P. Fornasiero and R. J. Gorte, *J. Am. Chem. Soc.*, , DOI:10.1021/jacs.0c00138.

127 A. Beniya, S. Higashi, N. Ohba, R. Jinnouchi, H. Hirata and Y. Watanabe, *Nat. Commun.*, 2020, **11**, 1888.

128 Y. Cai, Y. Guo and J. Liu, *Chem. Commun.*, 2020, **56**, 876–879.

129  S. Kattel, P. Liu and J. G. Chen, *J. Am. Chem. Soc.*, 2017, **139**, 9739–9754.

130  P. C. K. Vesborg and B. Seger, *Chem. Mater.*, 2016, **28**, 8844–8850.

131  A. S. Varela, W. Ju, A. Bagger, P. Franco, J. Rossmeisl and P. Strasser, *ACS Catal.*, 2019, **9**, 7270–7284.

132  S. Xu and E. A. Carter, *Chem. Rev.*, 2019, **119**, 6631–6669.

133  L. Wang, W. Chen, D. Zhang, Y. Du, R. Amal, S. Qiao, J. Wu and Z. Yin, *Chem. Soc. Rev.*, 2019, **48**, 5310–5349.

134  J. Graciani, K. Mudiyanselage, F. Xu, A. E. Baber, J. Evans, S. D. Senanayake, D. J. Stacchiola, P. Liu, J. Hrbek, J. F. Sanz and J. A. Rodriguez, *Science*, 2014, **345**, 546–550.

135  X. Chen, X. Su, H.-Y. Su, X. Liu, S. Miao, Y. Zhao, K. Sun, Y. Huang and T. Zhang, *ACS Catal.*, 2017, **7**, 4613–4620.

136  W. Lin, K. M. Stocker and G. C. Schatz, *J. Am. Chem. Soc.*, 2017, **139**, 4663–4666.

137  J. H. Kwak, L. Kovarik and J. Szanyi, *ACS Catal.*, 2013, **3**, 2449–2455.

138  P. A. U. Aldana, F. Ocampo, K. Kobl, B. Louis, F. Thibault-Starzyk, M. Daturi, P. Bazin, S. Thomas and A. C. Roger, *Catal. Today*, 2013, **215**, 201–207.

139  S. Li, Y. Xu, Y. Chen, W. Li, L. Lin, M. Li, Y. Deng, X. Wang, B. Ge, C. Yang, S. Yao, J. Xie, Y. Li, X. Liu and D. Ma, *Angew. Chem. Int. Ed.*, 2017, **56**, 10761–10765.

140  Y. Wang, H. Arandiyan, J. Scott, K.-F. Aguey-Zinsou and R. Amal, *ACS Appl. Energy Mater.*, 2018, **1**, 6781–6789.

141  S. Back, J. Lim, N.-Y. Kim, Y.-H. Kim and Y. Jung, *Chem. Sci.*, 2017, **8**, 1090–1096.

142  J. H. Kwak, L. Kovarik and J. Szanyi, *ACS Catal.*, 2013, **3**, 2094–2100.

143  J. C. Matsubu, S. Zhang, L. DeRita, N. S. Marinkovic, J. G. Chen, G. W. Graham, X. Pan and P. Christopher, *Nat. Chem.*, 2017, **9**, 120–127.

144  S. Yao, L. Lin, W. Liao, N. Rui, N. Li, Z. Liu, J. Cen, F. Zhang, X. Li, L. Song, L. Betancourt De Leon, D. Su, S. D. Senanayake, P. Liu, D. Ma, J. G. Chen and J. A. Rodriguez, *ACS Catal.*, 2019, **9**, 9087–9097.

145  B. Ravel, *J. Phys. Conf. Ser.*, 2009, **190**, 012026.

146  L. DeRita, J. Resasco, S. Dai, A. Boubnov, H. V. Thang, A. S. Hoffman, I. Ro, G. W. Graham, S. R. Bare, G. Pacchioni, X. Pan and P. Christopher, *Nat. Mater.*, 2019, **18**, 746–751.

147  H. Zhai and A. N. Alexandrova, *ACS Catal.*, 2017, **7**, 1905–1911.

148  L. B. Vilhelmsen and B. Hammer, *J. Chem. Phys.*, 2014, **141**, 044711.

149  P. C. Jennings, S. Lysgaard, J. S. Hummelshøj, T. Vegge and T. Bligaard, *Npj Comput. Mater.*, 2019, **5**, 46.

150  G. G. Rondina and J. L. F. Da Silva, *J. Chem. Inf. Model.*, 2013, **53**, 2282–2298.

151  R. B. Wexler, T. Qiu and A. M. Rappe, *J. Phys. Chem. C*, 2019, **123**, 2321–2328.

152  J.-X. Liu, Y. Su, I. A. W. Filot and E. J. M. Hensen, *J. Am. Chem. Soc.*, 2018, **140**, 4580–4587.

153  H. Guo, P. Sautet and A. N. Alexandrova, *J. Phys. Chem. Lett.*, 2020, **11**, 3089–3094.

154  B. Zandkarimi and A. N. Alexandrova, *J. Phys. Chem. Lett.*, 2019, **10**, 460–467.

155  G. Liu, P. Poths, X. Zhang, Z. Zhu, M. Marshall, M. Blankenhorn, A. N. Alexandrova and K. H. Bowen, *J. Am. Chem. Soc.*, , DOI:10.1021/jacs.0c01855.

156  S.-D. Huang, C. Shang and Z.-P. Liu, *J. Chem. Phys.*, 2019, **151**, 174702.

157  H. Zhai and A. N. Alexandrova, *J. Chem. Theory Comput.*, 2016, **12**, 6213–6226.

158  B. R. Goldsmith, J. Esterhuizen, J.-X. Liu, C. J. Bartel and C. Sutton, *AIChE J.*, 2018, **64**, 2311–2323.
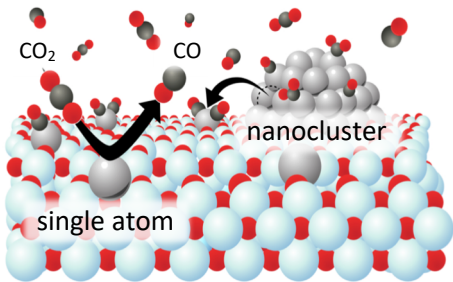
We highlight different aspects of single-atom and nanocluster catalysts for $CO_2$ reduction and CO oxidation, including synthesis, dynamic restructuring, and trends in activity and selectivity.